Effects of Arctic sea-ice concentration on turbulent surface fluxes in four atmospheric reanalyses

Tereza Uhlíková[1], Timo Vihma[2], Alexey Yu Karpechko[2], and Petteri Uotila[1]

[1]Institute for Atmospheric and Earth System Research, Faculty of Science, University of Helsinki, 00014, Helsinki, Finland
[2]Finnish Meteorological Institute, Helsinki, Finland

Correspondence: Tereza Uhlíková (tereza.uhlikova@helsinki.fi)

Abstract. A prerequisite for understanding the local, regional, and hemispherical impacts of Arctic sea-ice decline on the atmosphere is to quantify the effects of sea-ice concentration (SIC) on the turbulent surface fluxes of sensible and latent heat in the Arctic. We analyse these effects utilising four global atmospheric reanalyses: ERA5, JRA-55, MERRA-2, and NCEP/CFSR (CFSR and CFSv2), and evaluate their uncertainties arising from inter-reanalysis differences in SIC and in the sensitivity of the turbulent surface fluxes to SIC. The magnitude of the differences in SIC is up to 0.15, but typically around 0.05 in most of the Arctic over all four seasons. Orthogonal-distance regression and ordinary-least-square regression analyses indicate that the greatest sensitivity of both the latent and the sensible heat flux to SIC occurs in the cold season, November to April. For these months, using daily means of data, the average sensitivity is 400 W m^{-2} for the latent heat flux and over 800 W m^{-2} for the sensible heat flux per unit of SIC (change of SIC from 0 to 1), with the differences between reanalyses as large as 300 W m^{-2} for the latent heat flux and 600 W m^{-2} for the sensible heat flux per unit of SIC. The sensitivity is highest for the NCEP/CFSR reanalysis. Comparing the periods 1980–2000 and 2001–2021, we find that the effect of SIC on turbulent surface fluxes has weakened, owing to the increasing surface temperature of sea ice and the sea-ice decline. The results also indicate signs of decadal-scale improvement in the mutual agreement between reanalyses. The effect of SIC on turbulent surface fluxes arises mostly via the effect of SIC on atmosphere-surface differences in temperature and specific humidity, whereas, the effect of SIC on wind speed (via surface roughness and atmospheric-boundary-layer stratification) partly cancels out in the turbulent surface fluxes, as the wind speed increases the magnitude of both upward and downward fluxes.

1 Introduction

Interactive processes within the air-ice-ocean system play a key role in the rapid Arctic warming of the lower troposphere and sea-ice decline (Dai et al. (2002); Screen and Simmonds (2010); Serreze et al. (2009)). These processes are complex and challenging to represent in models, yet, to better understand the local, regional, and hemispherical impacts of Arctic sea-ice decline on the atmosphere, it is crucial to quantify the effects of sea-ice concentration (SIC) on turbulent surface fluxes in the Arctic.

The surface mass balance of sea ice (bare or snow-covered) is controlled by solar shortwave and thermal longwave radiative fluxes, turbulent surface fluxes of latent and sensible heat (LHF, SHF) as well as by conductive heat flux from the ocean through

ice and snow. According to observations, in winter, the cooling of the snow/ice surface due to negative net longwave radiation is balanced by downward SHF from air to ice and upward conductive heat flux (Persson et al. (2002); Walden et al. (2017)). By warming the snow/ice surface, SHF reduces the temperature gradient through the ice and snow, and accordingly, reduces the basal ice growth (Lim et al., 2022). In spring, downward longwave radiation is usually the most important factor triggering the onset of snow melt on top of sea ice (Maksimovich and Vihma, 2012), whereas in summer, downward solar radiation is mostly responsible for the surface melt of snow and ice (Tsamados et al., 2015).

Sea ice affects the climate system by regulating the exchange of momentum, heat, moisture, and other material fluxes between the atmosphere and the ocean, and by having much higher albedo than the open water. The difference in albedo between the sea ice and the ocean plays the most significant role during summer, when the sun is at its highest and the reduced albedo of the sea-ice-free water allows more absorption of the downward solar radiation that heats the ocean and, via the turbulent fluxes, the near-surface air (Perovich et al., 2007). The insulating effect of the sea ice is especially evident during winter and spring, when the ocean is considerably warmer than the atmosphere. Then the heat loss to the atmosphere mostly occurs in areas of open water; leads and polynyas. Leads are narrow, elongated openings of the ice cover typically generated by divergent ice drift, and they may be several tens of kilometres long and meters to kilometres wide (Alam and Curry, 1997). Polynyas are larger areas of open water generated either by sea-ice dynamics or anomalous oceanic heat flux melting the ice from below (Wei et al., 2021). The heat loss from leads and polynyas to the atmosphere is mostly governed by SHF, with smaller roles of LHF and net longwave radiation (Gultepe et al., 2003). The magnitude of upward LHF and SHF over these sea-ice openings is often ten to a hundred times larger than over the sea ice (Overland et al. (2000); Michaelis et al. (2021)), and wintertime observations have indicated the sum of SHF and LHF exceeding 500 W m^{-2} (Andreas et al., 1979). Hence, variations and climatological trends in SIC are critically important for the heat budget of the lower atmosphere and the upper ocean in the Arctic, and a key issue is to better understand and quantify the interactions of SIC and the surface turbulent fluxes.

From the point of view of modelling of the atmosphere, sea ice is a challenging surface type. SIC may change rapidly due to combined effects of dynamic and thermodynamic atmospheric and oceanic forcing (Aue et al., 2022). Due to these rapid changes and the challenges in sea-ice monitoring caused by the darkness during the polar night and prevailing cloud cover during summer, the information available on SIC is often inaccurate. Because of the optical challenges in the sea-ice monitoring, the information is mostly based on passive microwave remote sensing data from polar-orbiting satellites. However, as shown e.g. in Figure 7 in Valkonen et al. (2008), the same passive microwave data processed using different algorithms may result in differences on the order of 20 %, which adds to the uncertainty in the representation of the Arctic lower atmosphere in models.

Nevertheless, global atmospheric reanalyses provide the best available information in data-sparse regions such as the Arctic (Bosilovich et al. (2015); Gelaro et al. (2017); Kobayashi et al. (2015)), and are often relied upon in climate and climate-change research. These data sets aim to provide a physically consistent estimate of past states of the atmosphere with spatial and temporal resolutions that are uniform around the globe, and they are generated by assimilating atmospheric and surface observations with short-term weather forecasts using modern weather-forecasting models. While the differences between reanalyses' variables of SIC, LHF, and SHF have been demonstrated via comparisons against observations (Bosilovich et al. (2015); Graham et al. (2019)) and inter-comparisons between reanalyses (Collow et al. (2020); Graham et al. (2019); Lindsay et al. (2014)),

how much different reanalyses scatter in the relationships between SIC and surface turbulent fluxes is not known. To fill these knowledge gaps, we carry out an inter-comparison of four commonly-used major global atmospheric reanalyses: ERA5, JRA-55, MERRA-2, and NCEP/CFSR (CFSR and CFSv2), with a focus on their relationships between SIC, LHF, and SHF.

2 Material and Methods

The study region is the marine Arctic. We used data from the era of satellite measurements (1980–2021) as, compared to previous years, they provide more reliable and consistent information on the concentration of Arctic sea ice, which in turn also allows for more precise estimation of turbulent surface fluxes in reanalyses. The past 42 years were divided into two study periods: 1980–2000 and 2001–2021. According to HadCRUT5 data (Morice et al., 2021), the Arctic has already been warming more than the world for most years since 1980, though, the Arctic amplification phenomenon strengthened considerably shortly after 2000. Hence, the division into two study periods allowed us to compare the period of the recent strong Arctic amplification of climate warming to the period directly preceding this phenomenon. Each year was divided into four three-month seasons with regard to the annual cycle of the Arctic sea ice: (1) November–December–January, (2) February–March–April, (3) May–June–July, (4) August–September–October. November–December–January is represented by the months of high sea-ice extent, February–March–April by the months preceding and following the maximum sea-ice extent in March, February–March–April by the months with low sea ice extent, and August–September–October by the months surrounding the month of minimum sea-ice extent in September.

We worked with data from four reanalyses: ERA5 (Hersbach et al., 2023), JRA-55 (JMA, 2013), MERRA-2 (GMAO (2015a); GMAO (2015b)), NCEP/CFSR (Saha et al. (2010), Saha et al. (2011)), all covering the selected period 1980–2021. Under the term 'NCEP/CFSR', we included data from NCEP Climate Forecast System Reanalysis (CFSR; covering the period 1980–2010) and NCEP Climate Forecast System Version 2 (CFSv2; covering the period 2011–2021). Because these two data sets come in different horizontal spatial resolutions ($0.312°\times0.313°$ resp. $0.204°\times0.205°$), we unified them for the whole data set 'NCEP/CFSR' to $0.4°\times0.4°$ ($\sim$45 km grid cell) using bilinear interpolation. Besides this adjustment, we worked with the original horizontal spatial resolution of the remaining reanalyses, which vary between $\sim$31 km to $\sim$55 km (ERA5, resp. JRA-55). The update cycle of reanalyses' forecasts (temporal resolution) ranges from 1 to 6 hours (ERA5 and MERRA-2, resp. NCEP/CFSR). In our study, we used daily means of the data as they provide sufficient representation of synoptic-scale atmospheric and sea-ice processes for our needs while significantly decreasing the size of the data set. For an overview of the basic characteristics of the reanalyses see Table 1.

From each reanalysis, we utilized the following variables: sea-ice concentration (SIC), surface latent heat flux (LHF), surface sensible heat flux (SHF), specific humidity in 2 m (Q_{2m}), temperature in 2 m (T_{2m}), temperature at the surface (T_s), U-component of wind (u), and V-component of wind (v), both in 10m. The signs of both turbulent heat fluxes were assigned with regard to the surface - positive LHF referring to condensation and deposition, negative to evaporation and sublimation; positive SHF referring to the downward flux, negative to the upward flux. Because Q_{2m} is not archived in ERA5 data sets, we followed Eqs. (7.4, 7.5) from ECMWF (2016) to calculate it using the dew-point temperature and surface pressure. Subsequently, we

Table 1. Basic characteristics of utilized global atmospheric and coupled reanalyses.

	ERA5	**JRA-55**	**MERRA-2**	**NCEP/CFSR**
Reference	Hersbach et al. (2020)	Kobayashi et al. (2015)	Gelaro et al. (2017)	Saha et al. (2010) Saha et al. (2014)
Forecast model	IFS CY41R2	JMA GSM	GEOS 5.12.4	GFS (Atmospheric model) MOM4 (Ocean model)
Data assimilation system	4DVar	4DVar	3DVar	3DVar (Coupled forecast system)
Horizontal resolution	0.25°×0.25° ∼31 km	0.561°×0.563° ∼55 km	0.5°×0.625° ∼50 km	CFSR: 0.312°×0.313° CFSv2: 0.204°×0.205° This study: 0.4°×0.4°; ∼45 km
Original temporal resolution	1 h	3 h	1 h	6 h

obtained the temperature difference between 2-m height and the surface (T_{diff}) by subtracting T_s from T_{2m}, and calculated the wind speed (WS_{10m}) using u and v. To obtain the difference in specific humidity between the surface and 2-m height (Q_{diff}), we first computed specific humidity at the surface (Q_s) according to Iribarne and Godson (1973) using T_s. For calculation of Q_{diff}, we then subtracted Q_s from Q_{2m} as in the case of T_{diff} calculation.

Using data from each reanalysis, we studied bilateral relationships between turbulent heat fluxes LHF or SHF and SIC, and multilateral relationships between LHF (SHF), SIC, Q_{diff} (T_{diff}), and WS_{10m} – the three latter variables being selected based on the LHF and SHF bulk parameterisation. In reanalyses, the general bulk parameterisation of surface turbulent fluxes is grid-averaged, taking into account different surface types with different surface temperatures (Claussen (1991); Koster and Suarez (1992)). In our case, the different surfaces within a grid cell were the sea-ice and water, therefore the bulk formulae of grid-averaged LHF ($<$ LHF $>$) and SHF ($<$ SHF $>$) includes SIC as shown in (Vihma, 1995):

$$< \mathrm{LHF} > = \mathrm{V}\rho\ \mathrm{L_E}[\mathrm{SIC}(\mathrm{C_{HE,ice}}(\mathrm{q_a} - \mathrm{q_{s,ice}})) + (1 - \mathrm{SIC})(\mathrm{C_{HE,water}}(\mathrm{q_a} - \mathrm{q_{s,water}}))] \quad (1)$$

$$< \mathrm{SHF} > = \mathrm{V}\rho\ \mathrm{c_p}[\mathrm{SIC}(\mathrm{C_{HE,ice}}(\theta_\mathrm{a} - \theta_\mathrm{s,ice})) + (1 - \mathrm{SIC})(\mathrm{C_{HE,water}}(\theta_\mathrm{a} - \theta_\mathrm{s,water}))] \quad (2)$$

where V stands for the wind speed at the lowest atmospheric level of the model applied in each reanalysis, ρ for the air density, L_E for the latent heat of sublimation, c_p for the specific heat of the air, and C_{HE} for the turbulent exchange coefficients; (q_a - q_s) and (θ_a - θ_s) are the differences in potential temperature and specific humidity between the lowest atmospheric level and the surface. In our study (specifically in subsection 3.3), we apply true T_s and T_{2m} when studying their effect on SHF, because the adiabatic correction in a 2-m layer is negligible. Surface temperature over the water and both snow covered and bare sea ice is

Table 2. Representation of the sea ice in reanalyses.

	ERA5	JRA-55	MERRA-2	NCEP/CFSR
Sea-ice concentration (SIC)	Fractional, external dataset[1]	Binary[2], external dataset[1]	Fractional, external dataset[1]	Fractional, modelled (coupled)
Satellite input for SIC	SSM/I[3] + SSMIS[4] (1979-08/2007); SSMIS[4] (09/2007-)	SMMR[5] (-1987); SSM/I[3] (1987-)	AVHRR[6] (1982-2002), AVHRR[6] + AMSR-E[7] (2003-03/2006), SSMIS[4] (04/2006-)	SMMR[5] + SSM/I[3] (-1996); SSM/I[3] (1997-02/2000); SSM/I[3] + SSMIS[4]+ AMSR-E[7] + AMSR2[8] (03/2000-)
SST[9] for clearing the sea ice	3 °C	None	None	2.15 °C
Sea-ice thickness	1.5 m, fixed	2 m, fixed	N/A[10]	Modelled (coupled)
Snow on ice	None	None	None	Modelled (coupled)

[1] See text for details

[2] SIC $>$ 0.55 = 1, SIC $\leq$ 0.55 = 0

[3] Special Sensor Microwave/Imager

[4] Special Sensor Microwave Imager-Sounder

[5] Scanning Multichannel Microwave Radiometer

[6] Advanced Very-High-Resolution Radiometer

[7] Advanced Microwave Scanning Radiometer – Earth Observing System sensor

[8] The Advanced Microwave Scanning Radiometer 2

[9] Sea-surface temperature

[10] 7-cm ice layer for computing a prognostic ice surface temperature, which is then relaxed towards 273.15 K as a representation of the upward oceanic heat flux.

calculated from the surface energy budget in each reanalysis. Turbulent exchange coefficients (C_{HE}) depend on the roughness lengths for momentum, heat and moisture, and on the stratification of the atmospheric surface layer.

For the bilateral-relationship analysis, we utilised the orthogonal-distance regression (ODR; Boggs et al. (1988)). Because all variables in reanalyses include uncertainties, we theoretically considered the ordinary-least-square regression (OLSR), which assumes no errors in the independent variable, not optimal for this case. Additionally, we carried out tests on bilateral ODR and OLSR performance using data from several grid cells from each reanalysis and while we found 'nearly identical' (at least five decimal numbers identical) coefficients of determination (correlation coefficient squared, R^2) for both regression methods, importantly, the slopes of the regression lines varied considerably. This is attributable to the above-mentioned OLSR's assumption of no errors in the independent variable (x, in our case SIC) and therefore minimising the distance only for x data to the regression line, whereas ODR minimises the orthogonal distance between both x and y data (in our case y is LHF or SHF) and the regression line. Utilising the same above-described tests comparing ODR and OLSR performance for multilateral regression analysis, however, we found 'nearly identical' values for all slopes of the regression lines between LHF (SHF) and SIC, Q_{diff} (T_{diff}), and WS_{10m} for both ODR and OLSR. Values of R^2 for all and individual components of the multilateral regression were 'nearly identical' using both ODR and OLSR as well. Based on the findings that both methods yielded 'nearly identical' results for the multilateral regression analysis (using our reanalyses data), we decided to use OLSR for the multilateral

regression analysis in our work, as it requires much fewer computing resources to perform. We used linear model for both ODR and OLSR as we evaluated it as the most applicable for our purposes, being aware of some non-linearity in the SIC effect on Q_{2m} (T_{2m}) and LHF (SHF), as shown for near-surface air temperature e.g. in (Lüpkes et al., 2008), their Figure 4.

The statistical-significance testing of the results (slopes for LHF, SHF and their explanatory variables) was performed using Student's t-test (95 % confidence interval) with adjusted degrees of freedom (DF_{adj}) according to Eq. (31) from Bretherton et al. (1999):

$$DF_{adj} = T\frac{1 - R_1R_2}{1 + R_1R_2} \tag{3}$$

where T stands for number of days in one sample (in our case days in seasons in the periods of 1980–2000 and 2001–2021) and R_1 respectively R_2 for correlation coefficient for lag 1 auto-correlation of turbulent heat flux (LHF or SHF) and its explanatory variable (SIC).

Each reanalysis typically uses not only its own (1) data-assimilation system, (2) forecast model (as seen in Table 1), and often (3) different parameterisation schemes for subgrid-scale variables (such as turbulent fluxes), but also more or less (4) different atmospheric and surface observations, and (5) different representations of the sea ice. In Table 2, we describe the representation of sea ice in selected reanalyses, which can have a considerable effect on the modelling of the lower troposphere. External datasets (unspecified in Table 2) used as sources for SIC in ERA5, JRA-55, and MERRA-2 are follows. ERA5 uses data from OSI SAF (Ocean and Sea Ice Satellite Application Facility) by EUMETSAT (European Organisation for the Exploitation of Meteorological Satellites): version OSI SAF (409a) for January 1979 through August 2007, and OSI SAF oper for September 2007 onwards (Hersbach et al., 2020). In JRA-55, conditions for SIC are daily data from COBE-SST (Centennial In Situ Observation-based Estimates of the Variability of Sea Surface Temperatures and Marine Meteorological Variables) (Kobayashi et al. (2015); (Matsumoto et al., 2006)). MERRA-2 uses monthly data from CMIP (Coupled Model Intercomparison Project) as in Taylor et al. (2000) prior to 1982, data from OISST (Optimum Interpolation Sea Surface Temperature) by NOAA (National Oceanic and Atmospheric Administration) for 1982 to March 2006, and data from OSTIA (Operational Sea Surface Temperature and Ice Analysis) by the Met Office from April 2006 onwards (Gelaro et al., 2017).

3 Results

3.1 Differences in sea-ice concentration and surface turbulent fluxes

To illustrate the climatology in and differences between the four selected reanalyses in sea-ice concentration (SIC), latent heat flux (LHF), and sensible heat flux (SHF), we calculated Mean Biases of Daily Field Means (hereafter referred to as Mean Biases) between NCEP/CFSR and other reanalyses (ERA5, JRA-55, MERRA-2) in nine Arctic basins (Figure 1) in all seasons and the two study periods (Figures 2, 3, and S2). NCEP/CFSR appears to be the most realistic in terms of physical processes due to its modelled sea-ice thickness and the snow on top of sea ice (see more in subsection 3.4), however, we do not assume that it is the best reanalysis with respect to turbulent surface fluxes and use Mean Biases to present an overview and comparison of the typical values in all reanalyses. Mean values (temporal together with spatial) of NCEP/CFSR variables

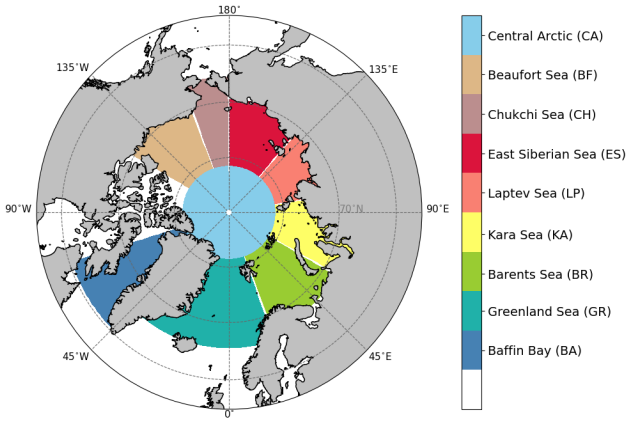

Figure 1. Arctic basins used for calculating daily field means of sea-ice concentration (SIC) and latent heat flux (LHF) in Tables 3, 4, S1, and Figures 2, 3, and S2.

Table 3. Mean sea-ice concentration in Arctic basins as represented in NCEP/CFSR in November–December–January (NDJ), February–March–April (FMA), May–June–July (MJJ), and August–September–October (ASO); in time periods 1980–2000 (I) and 2001–2021 (II).

Season	**NDJ**		**FMA**		**MJJ**		**ASO**	
Time period	I	II	I	II	I	II	I	II
Central Arctic	0.95	0.95	0.96	0.96	0.92	0.94	0.87	0.88
Beaufort Sea	0.65	0.64	0.65	0.65	0.57	0.56	0.48	0.39
Chukchi Sea	0.76	0.72	0.81	0.82	0.68	0.65	0.46	0.28
East Siberian Sea	0.81	0.80	0.81	0.81	0.72	0.71	0.56	0.35
Laptev Sea	0.42	0.42	0.41	0.42	0.34	0.33	0.24	0.15
Kara Sea	0.42	0.38	0.44	0.43	0.35	0.29	0.16	0.07
Barents Sea	0.30	0.20	0.39	0.32	0.24	0.17	0.06	0.03
Greenland Sea	0.15	0.14	0.17	0.17	0.12	0.13	0.07	0.06
Baffin Bay	0.24	0.21	0.32	0.31	0.18	0.17	0.02	0.01

in Arctic basins, seasons, and periods are shown in Tables 3, 4, and S1. The mean values of NCEP/CFSR variables in these Tables are not directly comparable with the values of Mean Biases of Daily Field Means between NCEP/CFSR and other reanalyses presented in Figures 2, 3, and S2 as the method of their calculation differs. However, looking at the Tables 3, 4, and S1 together with the Figures 2, 3, and S2 can provide an estimate of absolute values of SIC, LHF, and SHF in ERA5, JRA-55, and MERRA-2. For the calculations of both Mean Biases and mean values, we used land-sea masks provided by each reanalysis and only considered grid cells completely covered by the sea.

The mean SIC in NCEP/CFSR ranged from 0.01 in Baffin Bay in August–September–October in 2001–2021 to 0.96 in the

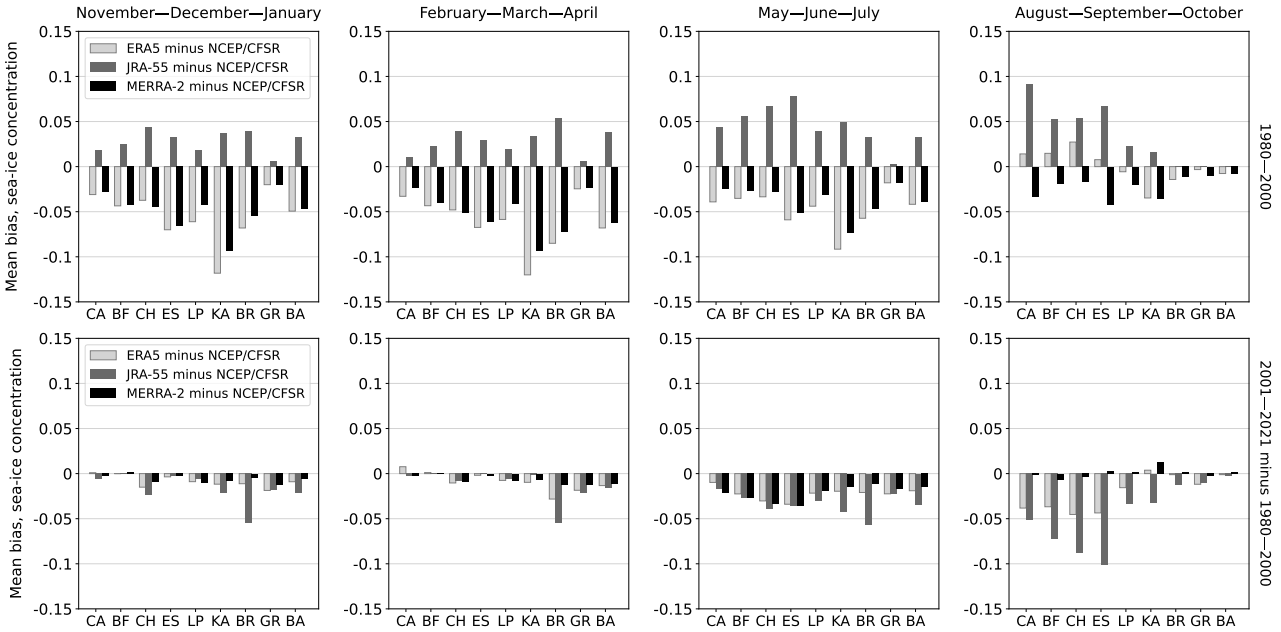

Figure 2. Mean Biases of Daily Field Means of sea-ice concentration: ERA5 minus NCEP/CFSR (light grey), JRA-55 minus NCEP/CFSR (grey), and MERRA-2 minus NCEP/CFSR (black). Horizontal axis refers to Arctic basins as seen in Figure 1. The first row shows data from period 1980–2000 and the second row the 2001–2021 difference from the earlier period. Only grid cells fully covered by the sea were considered in this analysis.

Table 4. Mean latent heat flux (W m^{-2}) in Arctic basins as parameterised in NCEP/CFSR in November–December–January (NDJ), February–March–April (FMA), May–June–July (MJJ), and August–September–October (ASO); in time periods 1980–2000 (I) and 2001–2021 (II).

Season	**NDJ**		**FMA**		**MJJ**		**ASO**	
Time period	I	II	I	II	I	II	I	II
Central Arctic	-4	-3	-2	-2	-12	-14	-11	-9
Beaufort Sea	-1	-1	-2	-1	-7	-8	-9	-8
Chukchi Sea	-9	-11	-4	-4	-8	-10	-17	-17
East Siberian Sea	-2	-2	-2	-2	-9	-10	-11	-10
Laptev Sea	-1	-1	-1	-2	-5	-5	-6	-7
Kara Sea	-5	-8	-3	-5	-6	-5	-9	-10
Barents Sea	-44	-44	-33	-37	-14	-13	-26	-23
Greenland Sea	-43	-40	-38	-36	-13	-13	-23	-21
Baffin Bay	-16	-18	-11	-12	-5	-5	-10	-11

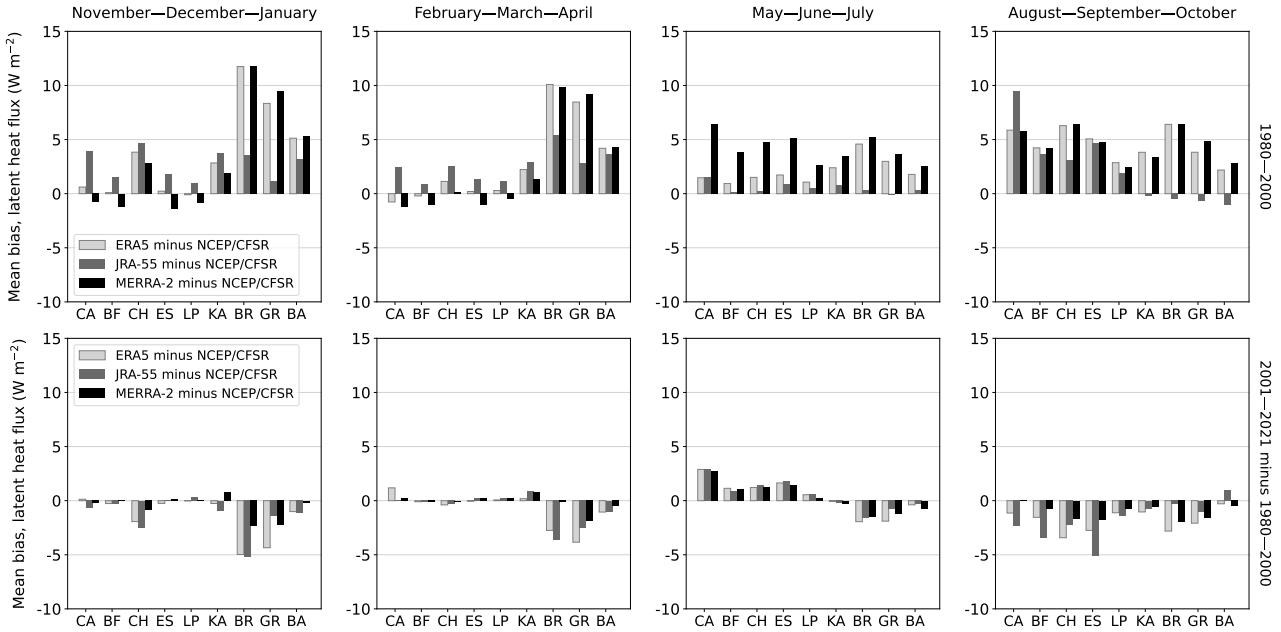

Figure 3. Mean Biases of Daily Field Means of latent heat flux: ERA5 minus NCEP/CFSR (light grey), JRA-55 minus NCEP/CFSR (grey), and MERRA-2 minus NCEP/CFSR (black). Horizontal axis refers to Arctic basins as seen in Figure 1. The first row shows data from period 1980–2000 and the second row the 2001–2021 difference from the earlier period. Only grid cells fully covered by the sea were considered in this analysis.

Central Arctic in February–March–April in both 1980–2000 and 2001–2021 (Table 3). The value of mean SIC decreased in nearly all basins between the periods 1980–2000 and 2001–2021: by 2 to 33 % in November–December–January, 2 to 18 % in February–March–April, 1 to 29 % in May–June–July, and 14 to 56 % in August–September–October. On the contrary, it increased or remained the same between the two study periods in the Central Arctic (in all seasons), and several other basins in February–March–April, by up to 2 %.

The Mean Biases between NCEP/CFSR and other reanalyses in SIC (calculated as a reanalysis minus NCEP/CFSR; Figure 2) were in nearly all regions and seasons in 1980–2000 between -0.1 and +0.05 SIC, with mostly negative Mean Biases between NCEP/CFSR and ERA5, and NCEP/CFSR and MERRA-2, and mostly positive Mean Biases between NCEP/CFSR and JRA-55. For most of the data in 1980–2000, the differences between ERA5 and JRA-55 were the largest, up to 0.15 in the Kara Sea in November–April, while the differences between ERA5 and MERRA-2 were the lowest. In the cold season (November–April), SIC in JRA-55 had in most cases lower magnitude of Mean Biases from NCEP/CFSR than ERA5 and MERRA-2. This was an interesting result, because JRA-55 has a binary representation of SIC (assigning value 1 for over 0.55 of SIC in a grid cell, and 0 for equal or less than 0.55), as opposed to nearly all concentrations being considered in other reanalyses (ranging from 0 to 1 in MERRA-2 and from 0.15 to 1 in ERA5 and NCEP/CFSR). The magnitude of Mean Biases between NCEP/CFSR and JRA-55 mostly decreased in 2001–2021, while between NCEP/CFSR and ERA5, and NCEP/CFSR

and MERRA-2, it increased in many basins, especially in May–June–July.

We found the mean LHF in NCEP/CFSR to be negative in all basins, seasons, and both periods (Table 4), with the smallest magnitude of the mean flux in the Laptev and Beaufort Seas (-1 W m^{-2}) and largest in the Barents Sea (-44 W m^{-2}), all in November–December–January. Corresponding to the changes in the mean SIC between the two study periods, in the cold season (November–April), the mean negative LHF intensified in the majority of basins with decreased SIC. Values of Mean Bias in LHF between NCEP/CFSR and other reanalyses took place mostly between -5 and +10 W m^{-2} (Figure 3). As in the case of SIC, Mean Biases between NCEP/CFSR and ERA5, and NCEP/CFSR and MERRA-2 were the highest, while differences between ERA5 and MERRA-2 were the lowest for most basins and seasons. The most noticeable results in the period 1980–2000 were large positive Mean Biases during November–April in the Barents and Greenland Seas between NCEP/CFSR and ERA5, and NCEP/CFSR and MERRA-2. These findings were not consistent with the theoretical expectations – negative Mean Biases in SIC being followed by negative Mean Biases in LHF (less sea ice resulting in more evaporation/sublimation than in NCEP/CFSR). However, as we will show in the Section 3.2 (Figures 4 and S4), in November–April, the correlations of SIC/LHF in ERA5 and MERRA-2 are not of a different sign from NCEP/CFSR and do follow the theoretical expectations for this relationship. Because the sea ice covers only a small part of the Greenland and Barents Sea basins (even in November–April) and we calculated the mean surface turbulent fluxes and Mean Biases using the whole extent of each basin as shown in Figure 1, smaller magnitude of the negative LHF in ERA5 and MERRA-2 compared to NCEP/CFSR are likely due to the differences in other factors affecting LHF (see Eq. (1)) in the ice-free areas of these basins. As to the Mean Biases in LHF in 2001–2021 between NCEP/CFSR and ERA5, JRA-55, or MERRA-2, their magnitudes mostly decreased in nearly all basins and seasons, compared to 1980–2000.

The mean SHF in NCEP/CFSR ranged from 0 W m^{-2} in the Kara Sea in February–March–April 2001–2021 to -49 W m^{-2} in the Barents Sea in November–December–January 1980–2000 (Table S1). Mean Biases in SHF between NCEP/CFSR and other reanalyses (Figure S2) ranged mostly between +10 W m^{-2} and -20 W m^{-2} in November–April, and between +5 W m^{-2} and -10 W m^{-2} in May–October. We found the largest magnitude of Mean Biases between NCEP/CFSR and ERA5, and NCEP/CFSR and MERRA-2, in November–April (over -20 W m^{-2} for MERRA-2 data in the Central Arctic in November–December–January). As in the case of LHF, in the Atlantic sector of the Arctic Ocean in November–April, negative Mean Biases in SIC (Figure 2) were accompanied by positive Mean Biases in SHF (Figure S2). Also in this case, the explanation of this seemingly non-physical relationship from the previous paragraph applies. Additionally, we show in Section 3.2 (Figures 6 and S7) that in November–April the SIC/SHF correlation is also of the same sign within all four reanalyses in our study. Similarly to Mean Biases in LHF, magnitude of differences between reanalyses decreased to some extent in most basins in 2001–2021 compared to 1980–2000.

3.2 Effect of sea-ice concentration on surface turbulent fluxes

To investigate the relationships between Arctic SIC and surface turbulent fluxes in reanalyses data, we first carried out bilateral orthogonal-distance-regression (ODR) analyses between SIC, LHF and SIC, SHF. For these analyses, we only included data (grid cells) with the mean of SIC > 0.5 in each period and season.

In Figure 4, we illustrate the change in LHF (W m^{-2}) per unit of SIC (slope of the regression line) in November–December–January in the periods 1980–2000, 2001–2021, and the difference of 2001–2021 from 1980–2000. The relationship between SIC and LHF in the Arctic in these months showed solely positive correlation (shades of red in Figure 4: a–h) meaning less sea ice – more evaporation/sublimation. This finding was consistent with the theoretical expectations: large amounts of moisture being released to the dry winter Arctic air from the (relatively) warm ocean when it is exposed by the sea ice retreat. Although the direction of the relationship was the same in all four reanalyses, there were differences in its strength. While we found the slopes of regression lines between SIC and LHF to be around 200–300 W m^{-2} LHF per unit of SIC (change of SIC from 0 to 1) in ERA5, JRA-55 and MERRA-2, we observed values up to 600 W m^{-2} LHF per unit of SIC in NCEP/CFSR data, indicating much higher sensitivity of LHF to SIC in the marine Arctic in this reanalysis (further addressed and explained in subsection 3.4). The large dark grey areas in the JRA-55 results (Figure 4: b, f, j) indicate a failure of the linear bilateral ODR model, caused by the binary representation of SIC in this reanalysis. Because the SIC in these dark grey areas was never less than 0.55 during the 21-year periods, every grid cell was assigned a value of 1, making it impossible for the model to explain the variations in LHF by variations in SIC. In other reanalyses, the dark grey areas appear as well, analogically, due to very low SIC variability in some regions (further addressed and explained later in this subsection and in Figures 6 and 7).

A positive correlation between SIC and LHF could also be observed in February–March–April and August–September–October (shades of red in Figures S4 and S6: a–h), with generally stronger relationship between the variables than in November–December–January. In May–June–July, however, the relationship between SIC and LHF turned into a negative correlation in most areas, meaning less sea ice – less evaporation (shades of blue in Figure S5: a–h). In this season, we found the strongest SIC/LHF relationship in the Central Arctic (north of 81.5 °N) for all reanalyses, ranging from around 300 W m^{-2} MERRA-2, to 400–600 W m^{-2} in ERA5 and NCEP/CFSR. The negative correlation between SIC and LHF in May–June–July can be explained as follows. Based on various SIC thresholds, the reanalyses keep the sea-surface temperature relaxed to the approximate sea-water freezing point (-1.8 °C) throughout the year (e.g. in Ishii et al. (2005), Good et al. (2020)), often resulting in the open water being colder than melting snow/ice in summer with the surface temperature at 0 °C (Persson et al. (2002); Vihma et al. (2008); Walden et al. (2017)). Accordingly, the surface temperatures favor less evaporation over the open water than over melting sea ice.

The effect of SIC on LHF in all seasons (as parameterised in reanalyses) weakened between the two periods for most of the Arctic (shades of blue in Figures 4, S4, S6: i–l; shades of red in Figure S5: i–l). To interpret this change, we produced Figure 5, which shows that the surface temperature (T_s) has risen nearly everywhere in the marine Arctic between 1980–2021 (row x). The strongest surface warming in the Barents, Kara, Laptev, and Chukchi Seas can be attributed to the sea ice being to a large extent replaced by the warmer sea (see the areas of strongest sea-ice decline in row xi). The warming in other areas (including the Central Arctic, where the mean SIC in 1980–2021 was 0.9–1, see row ix) indicates warming of the sea-ice surface in past decades. Based on these findings, we present the following explanations on why the SIC/LHF relationship weakened between the two study periods: (1) For the leads opening in otherwise mostly compact sea ice: the surface temperature of the sea ice has increased while the underlying sea temperature remained the same (at the sea-water freezing temperature of approximately -1.8 °C), hence, the difference in the surface saturation specific humidities between the sea ice and open water decreased, directly

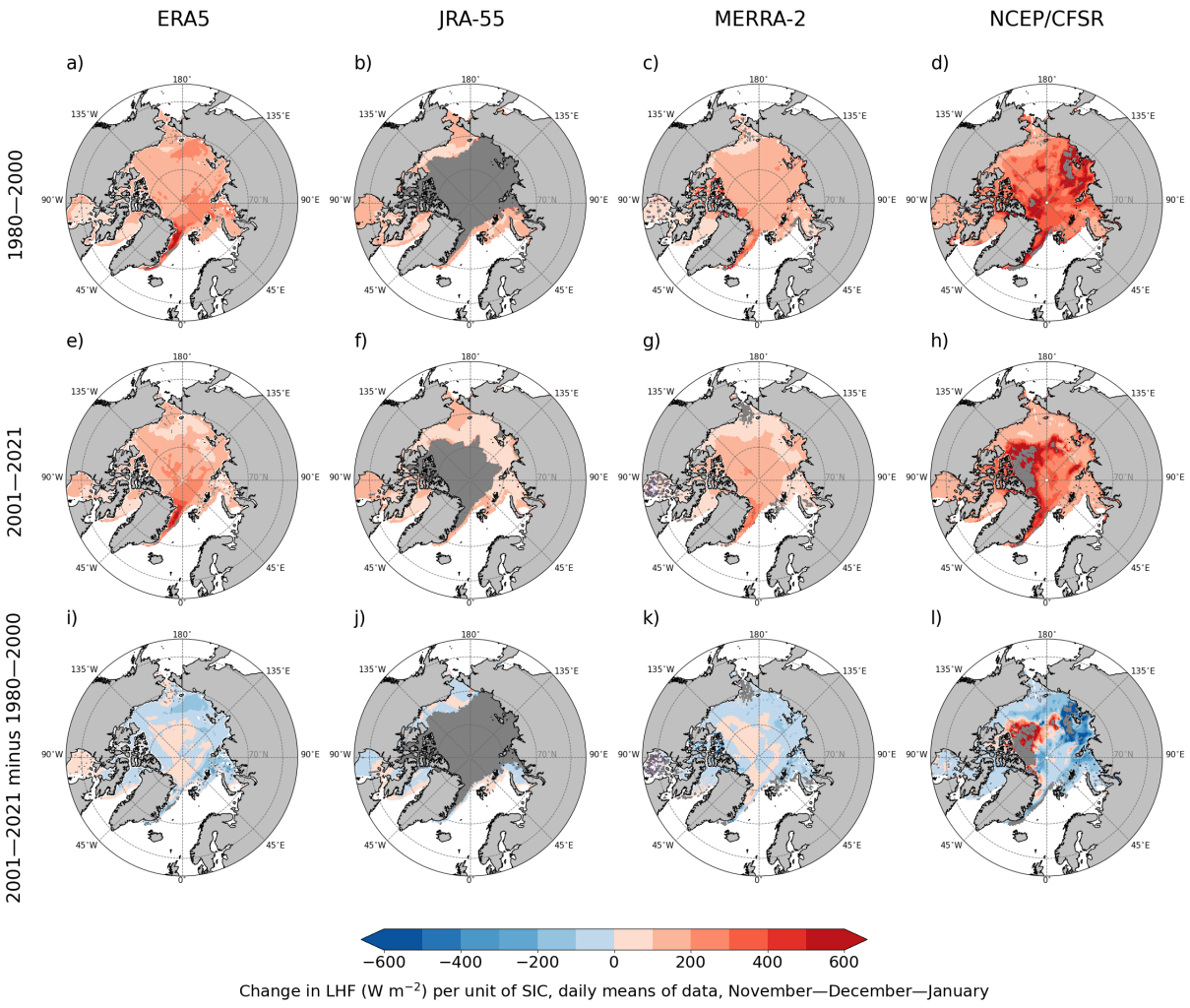

Figure 4. Change in latent heat flux (W m^{-2}) per unit of change in sea-ice concentration (slope of regression line) in four reanalyses (columns), marine Arctic, November–December–January, based on the linear orthogonal-distance-regression (ODR) model. **a–d** depict the period 1980–2000, **e–h** period 2001–2021, and **i–l** show the 2001–2021 difference from 1980–2000. Dark grey indicates areas where the ODR model did not converge; in i–l, dark grey shows these areas in 1980–2000 and/or 2001–2021. Only grid cells with a mean of SIC > 0.5 were considered, and only statistically significant results within 95 % confidence interval are shown.

contributing to a decreased sensitivity of LHF to SIC; (2) The sea ice has declined considerably or disappeared completely from some of the grid cells, therefore there is very small to no SIC effect on LHF in the latter study period. Mostly in the Central Arctic, however, we found some areas of increased SIC effect on LHF between 1980–2000 and 2001–2021 (shades of red in Figures 4, S4, S6: i–l; shades of blue in Figure S5: i–l, meaning a stronger relationship in 2001–2021). This increased

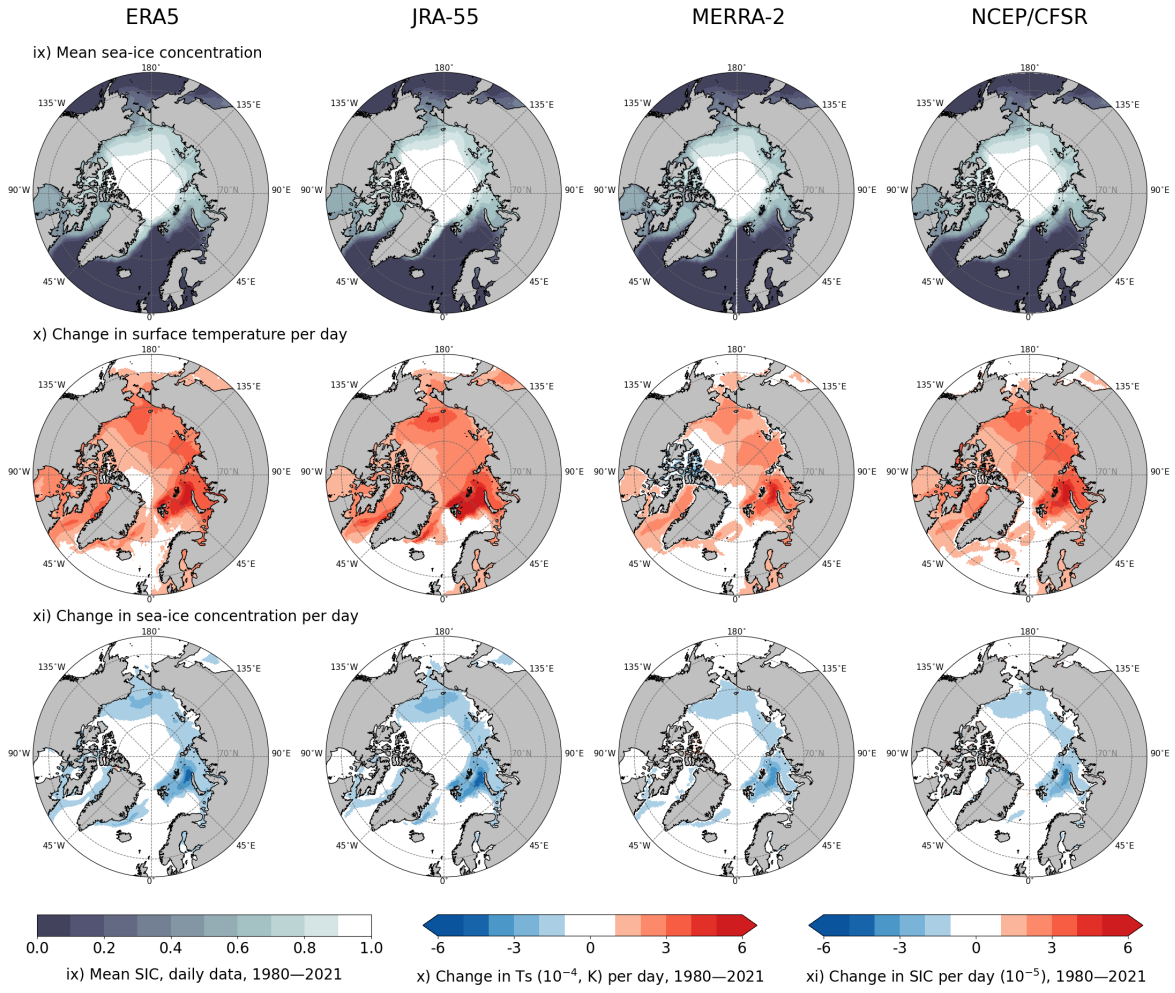

Figure 5. Mean sea-ice concentration (row **ix**), change of surface temperature per day (row **x**), and change in sea-ice concentration per day (row **xi**); 1980–2021, daily means of data in four reanalyses. Changes in variables per day are slopes of ordinary-least-square-regression line using time as an independent variable.

SIC effect on LHF may be explained as follows. As mentioned before, the effect of SIC on near-surface air temperature (and specific humidity) is not linear, but it is usually the strongest with leads opening in SIC very close to 1. As indicated in Table 3 and shown in our representative grid cells (Figure S3), SIC in some areas of the Central Arctic increased between 1980–2000 and 2001–2021 (possible reasons discussed in subsection 4.5). Therefore, there has been mostly very high SIC in 2001–2021, where even very small decrease in SIC has a strong effect on near-surface air temperature and specific humidity. We cannot be sure, however, whether SIC increased in reality in these parts of the Central Arctic in 2001–2021 compared to 1980–2000, and

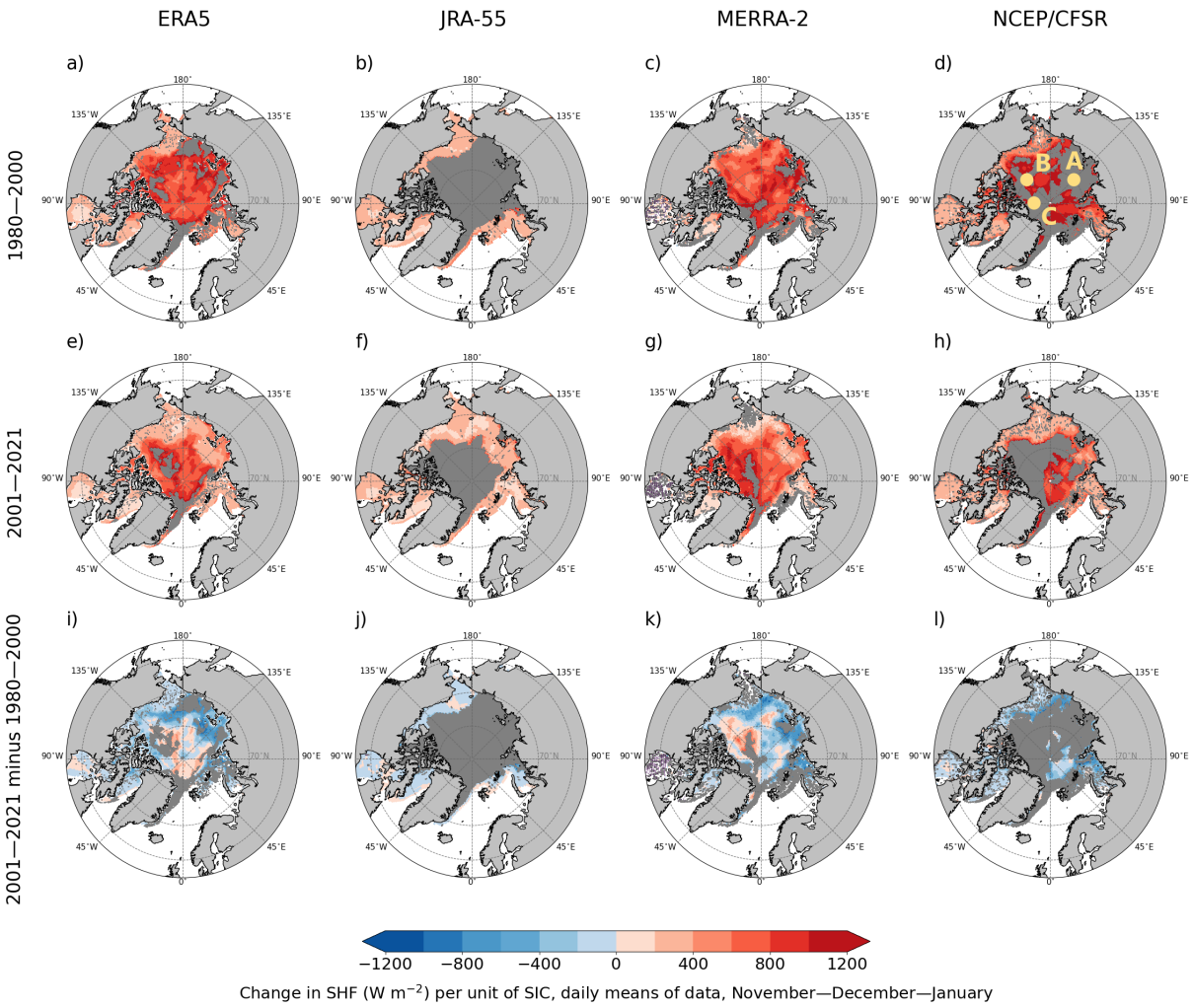

Figure 6. Change in sensible heat flux (W m^{-2}) per unit of change in sea-ice concentration (slope of regression line) as represented in four reanalyses (columns), marine Arctic, November–December–January, based on the linear orthogonal-distance-regression (ODR) model. **a–d** depict the period 1980–2000, **e–h** period 2001–2021, and **i–l** show the 2001–2021 difference from 1980–2000. Dark grey indicates areas where the ODR model did not converge; in i–l, dark grey shows these areas in 1980–2000 and/or 2001–2021. Points A, B, C from **d** are further analysed in Figure 7. Only grid cells with a mean of SIC > 0.5 were considered, and only statistically significant results within 95 % confidence interval are shown.

only comment on possible physical and statistical explanations of the phenomena as represented in reanalyses data.

Also for SHF, the change in the flux per unit of SIC (slope of the regression line) depended on the season, region, and decadal period (Figures 6, S7–S9). As in the case of SIC/LHF relationship, SIC and SHF were positively correlated in the

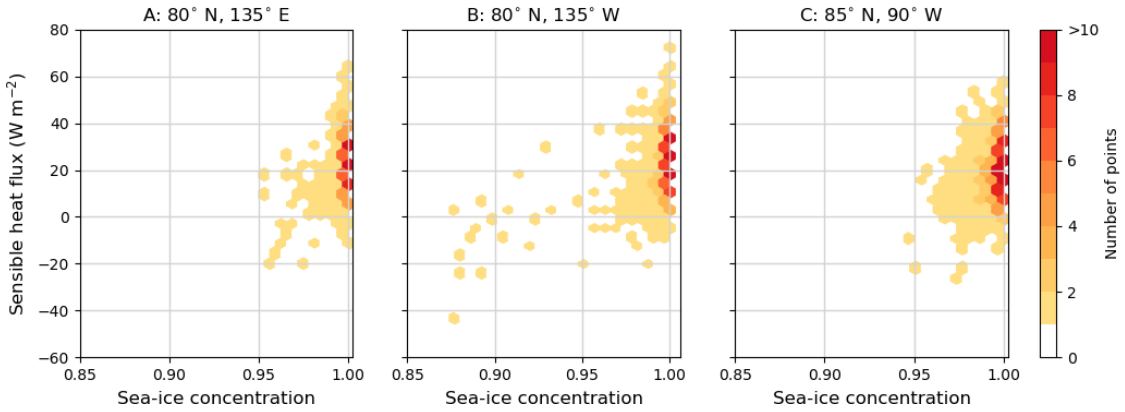

Figure 7. Daily sea-ice concentration and sensible heat flux in three selected grid cells from dark-grey areas indicated in Figure 6, NCEP/CFSR data, days in November–December–January months in 1980–2000 (1932 days). **A**: Grid cell nearest to 80° N, 135° E; **B**: Grid cell nearest to 80° N, 135° W; **C**: Grid cell nearest to 85° N, 90° W.

Arctic in November–December–January (shades of red in Figure 6: a–h), meaning less sea ice – more upward (negative) SHF. These results are also consistent with the theoretical expectations, as mentioned above: the sea is considerably warmer than the near-surface air in the cold seasons (November–April) and, when the insulating sea-ice layer retreats, a large amount of upward SHF is released. The strength of the SIC/SHF correlation ranged from around 300 W m^{-2} SHF per unit of SIC in JRA-55 data (keeping in mind the limited area where it was possible to analyse the relationship) to around 800 W m^{-2} SHF per unit of SIC in ERA5, NCEP/CFSR, and MERRA-2. Similarly to SIC/LHF, there were dark grey areas (grid cells) in our results of SIC/SHF regression analysis, where the linear bilateral ODR model did not converge. As we mentioned above, in the case of JRA-55 (Figure 6: b, f, j), the failure of the model was caused by the binary representation of SIC in this reanalysis which makes it impossible for the model to explain the variations in LHF or SHF by variations in SIC. In Figure 7, using grid cells from dark grey areas from NCEP/CFSR data, we show that in cold seasons, the reason for the model failure is similar also in reanalyses with fractional representation of SIC – very low SIC variability and high SHF variability. In these selected grid cells the SIC mostly varied only between 0.95 and 1, while SHF showed variability between -20–60 W m^{-2}. On most days (highest density of points, darkest orange/red), the SIC was 1 and SHF 0–30 W m^{-2}, resulting in no clear bilateral relationship.

Comparably with the SIC/LHF relationship, we also found positive correlation for SIC/SHF in February–March–April and partly August–September–October (shades of red in Figures S7 and S9: a–h). The areas where the linear ODR model did not converge expanded considerably in February–March–April compared to November–December–January, probably due to less variation in SIC during February–March–April (before the melting starts) compared to November–December–January (with the sea typically just starting to freeze in November). The fact that there are more dark-grey areas in Figures 6 and S7 (SIC/SHF relationship, November–April) than Figures 4 and S4 (SIC/LHF relationship, November–April) can be attributed to greater variability in SHF than LHF in the Arctic during these seasons, making it harder for the model to fit a regression line when SIC is very high. In May–June–July, the SIC/SHF relationship also turned into a negative correlation (shades of blue

in Figure S8), meaning less SIC – more downward (positive) SHF. We observed similar spatial distribution of the correlation strength as in SIC/LHF results for May–June–July, with the maximum slope of the regression line in the Central Arctic (around 400 W m^{-2} per unit of SIC in ERA5 and MERRA-2, and up to 800 W m^{-2} per unit of SIC in NCEP/CFSR). The summer change of the slope sign can be explained analogically to the SIC/LHF relationship: the open water at the sea-water freezing point (-1.8 °C) is colder than the summer ice surface temperature at about the snow/ice melting point (0 °C). Therefore opening leads (less sea ice) induces more downward (positive) SHF in reanalyses.

The SIC effect on SHF weakened between 1980–2000 and 2001–2021 in most of the Arctic and strengthened in some parts of the Central Arctic and Beaufort Sea across all the seasons (shades of blue in Figures 6, S7, S9: i–l; shades of red in Figure S8: i–l), very similarly to the SIC/LHF relationship. The same explanation of this trend is valid for the change in SIC/SHF relationship: Increasing surface temperature of the sea ice reduces the surface temperature difference between ice and water, directly contributing to lower sensitivity of SHF to SIC. The stronger relationship between SIC and SHF in Central Arctic and Beaufort Sea in 2001–2021 compared to 1980–2000 (shades of red in Figures 6, S7, S9: i–l; shades of blue in Figure S8: i–l) can be explained in similar terms as the increased SIC effect on LHF earlier in this subsection.

3.3 Multiple drivers of surface turbulent fluxes

To assess more drivers of the surface turbulent fluxes in reanalyses (as shown in the fluxes' bulk parameterisation in Eqs. (1) and (2)), we further performed linear multilateral ordinary-least-square regression (OLSR) analyses utilizing SIC, specific-humidity difference (Q_{diff}, Q_{2m} minus Q_s), and wind speed in 10m (WS_{10m}) as explanatory variables for variance in LHF; and SIC, temperature difference (T_{diff}, T_{2m} minus T_s), and wind speed in 10m (WS_{10m}) as explanatory variables for SHF variance. As an outcome of these analyses, we studied the variance in LHF or SHF (vLHF, vSHF) explained by the model (coefficient of determination, R^2) overall, and the proportion of the overall R^2 explained by each of the three drivers mentioned above.

Besides the decline in the sea-ice extent, we found both the overall and partial values of R^2 in 1980–2000 quantitatively very similar to those in 2001–2021 within all reanalyses, seasons and both LHF and SHF (Figures 8, S10–S24).

During the cold season (November–April), the model explained around 80 % of vSHF, with similar spatial distribution in ERA5, JRA-55, and MERRA-2 (Figures 8, S10-S12). The partial R^2 also had similar values within these three reanalyses – around 20 % vSHF explained by SIC, around 50 % explained by T_{diff}, and around 10 % by WS_{10m}. In NCEP/CFSR in November–April, however, nearly everywhere outside of the marginal-ice zone, the model explained only around 40–50 % vSHF overall. While in these regions, the partial R^2 explained by SIC and WS_{10m} had about the same values as in the remaining three reanalyses, the partial R^2 for T_{diff} only reached values around 20–30 %. During the warm season (May–October; Figures S13–S16), however, both overall and partial R^2 in NCEP/CFSR were about the same as in other reanalyses (about 70–80 % overall, around 10 % for SIC, 60 % for T_{diff}, and mostly <10 % for WS_{10m}). Hence, the cold-season difference in NCEP/CFSR results are likely due to the role of snow on the sea ice (which is existing and modelled in this reanalysis unlike in the other ones). Insulation by snow causes lower T_s because it reduces upward conductive heat flux from the ocean under the sea ice to the snow surface. Lower T_s reduces T_{diff} in very cold November–April conditions in the Arctic. At the same time, when a lead opens, the difference between T_s of the snow and T_s of the water is much larger than the difference between the T_s of bare sea

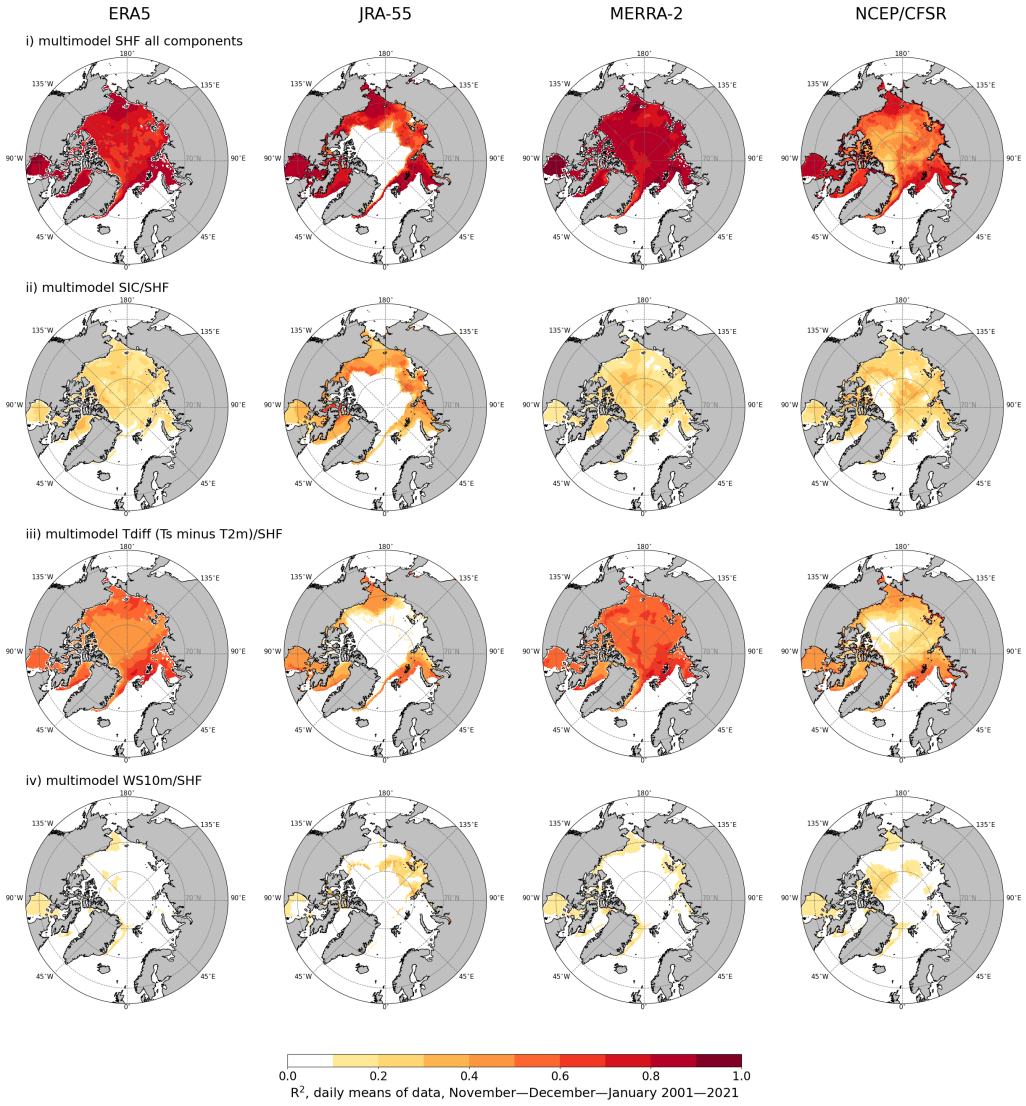

Figure 8. Proportion of variance in the sensible heat flux (vSHF) explained by the linear ordinary-least-square regression model (coefficient of determination, R^2); daily means of data, November–December–January, 2001–2021. Row **i** - vSHF explained by all components: SIC/temperature difference (T_{2m} minus T_s, T_{diff})/wind speed (10 m, WS_{10m}); row **ii** - vSHF explained by the SIC/SHF component of the model; row **iii** - vSHF explained by the T_{diff}/SHF component of the model; row **iv** - vSHF explained by the WS_{10m}/SHF component of the model. Only grid cells with a mean of SIC > 0.5 were considered.

ice and water, resulting in larger magnitude of upward SHF than in the case of bare sea-ice surface compared to open water. In November–April, this should make variance in SIC more important in explaining vSHF to account for the lower importance of T_{diff} in NCEP/CFSR than the remaining reanalyses. However, according to our results in Figures 8, S10–S12, this was mostly not the case. As we presented for bilateral relationships between SIC and SHF in Figures 6 and S7, the linear ODR model using NCEP/CFSR data did not converge in large areas of the marine Arctic in November–December–January and even larger areas in February–March–April presumably due to very low variability in the SIC and large variability in SHF, which points to the difficulty faced by this kind of model in reproducing cold-seasons surface and near-surface-air conditions using NCEP/CFSR data.

The vLHF explained by the linear multilateral OLSR in warm season (May–October; Figures S21–S24) was very similar to that for vSHF for both study periods and all reanalyses – around 80 % overall, around 10–20 % for SIC, 50–60 % for Q_{diff}, and around 10 % for WS_{10m}. In November–April (Figures S17–S20) in NCEP/CFSR results, we also came across lower overall (and Q_{diff}) R^2 – around 40 % (and <10 %) in the areas of SIC/LHF linear model failure. In other reanalyses in November–April, the overall vLHF explained by the model had about the same values as in the case of vSHF, although, the partial R^2 for SIC were higher (around 40 % in November–December–January and around 30 % in February–March–April) and the partial R^2 for Q_{diff} accordingly lower. Variations in WS_{10m} explained on average more vLHF than vSHF – around 10–20 %.

3.4 Thin ice on leads and snowpack on top of sea ice

In addition to the effects of SIC on turbulent fluxes, there are two factors that deserve particular attention: the effects of thin ice on leads and the effects of the snowpack on top of sea ice.

Considering the first one, reanalyses assume that the open parts of each grid cell have the surface temperature at the freezing point of ocean water, -1.8 °C. However, in reality winter leads typically remain open for less than a day (Makshtas, 1991) or just a few hours (Petrich et al., 2007) and are thereafter covered by thin ice with the surface temperature lower than -1.8 °C. This results in reanalyses overestimation of upward turbulent fluxes arising from leads. To estimate the magnitude of the overestimation, we carried out analytical calculations. We focused on the cold season when the insulating effect of the ice layer is largest, so that the results represent the maximum effect of thin ice on leads. As a first approximation, we assume that the temperature profile through a thin ice layer is linear. Then the conductive heat flux C is:

$$C = -k_i\,(T_s - T_b)/\,h_i \tag{4}$$

where k_i stands for the heat conductivity of ice, T_s for ice surface temperature, T_b for the ice bottom temperature (-1.8 °C), and h_i for the ice thickness. The turbulent fluxes of sensible and latent heat were calculated applying the standard bulk formulae (analogous to Eqs. (1) and (2), but here for local instead of grid-averaged fluxes):

$$LHF = V\rho\, L_E C_{HE}(q_a - q_s) \tag{5}$$

$$SHF = V\rho\, c_p C_{HE}(T_a - T_s) \tag{6}$$

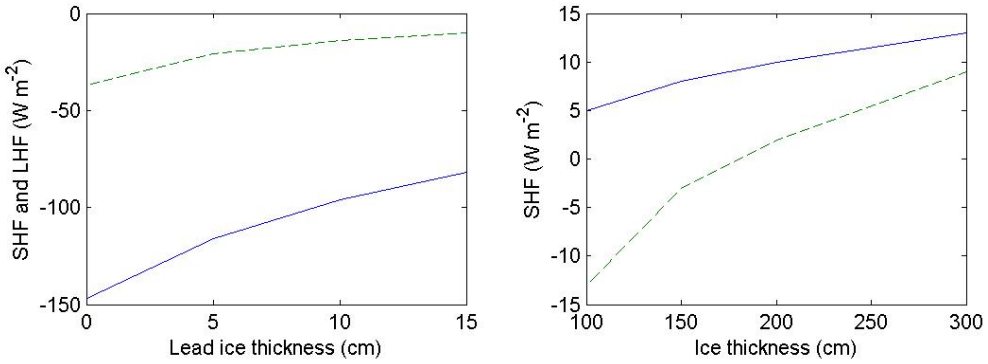

Figure 9. a: Effect of lead ice thickness on SHF (solid line) and LHF (dashed line) on leads, and **b**: effect of snow on top of thick sea ice - SHF in case of 20 cm snow pack on ice (solid line) and bare ice (dashed line). The fluxes are calculated for February conditions as observed at the drifting ice station SHEBA (Persson et al., 2002).

The upward long-wave radiation (ULW) was calculated as:

$$\mathrm{ULW} = -\sigma\ \mathrm{T_s}^4 \tag{7}$$

where σ stands for the Stefan-Boltzmann constant (5.67×10^{-8} W m^{-2} K^{-4}). The downward longwave radiation (DLW) and the input for Eqs. (4) to (7) was taken from observations in the central Arctic during the SHEBA campaign (Persson et al., 2002) in February, when the mean values were following: 155 W m^{-2} for DLW, 5.0 m s^{-1} for V, -32 °C for T_a, 0.9 for relative humidity, yielding 0.17 g kg^{-1} for q_a, and 2.1 W m^{-1} K^{-1} for k_i. The LHF and SHF were first calculated for open leads, using Eqs. (5) and (6) with T_s set to -1.8 °C. Then the calculations were repeated assuming different values for h_i: 0.05, 0.1, and 0.15 m. As T_s is unknown and all the fluxes except DLW depend on it, different T_s values were given until the net heat flux (sum of radiative, turbulent and conductive fluxes) became zero, representing equilibrium conditions. The dependence of SHF and LHF on the thickness of the lead ice is shown in Figure 9 a. Compared to an open lead, already 0.05 m of ice reduced the magnitude of SHF from 147 to 116 W m^{-2}, and further to 82 W m^{-2} when the ice thickness reached 0.15 m. As expected, the flux magnitudes and their sensitivity to ice thickness are qualitatively similar but smaller for LHF.

Considering the effects of snowpack on top of thick sea ice, ignored in ERA5 and JRA-55, we again applied SHEBA climatology for February, and calculated the equilibrium net flux and its components for cases of bare and snow-covered sea ice, for a constant snow depth of 0.2 m and ice thicknesses of 1.0, 1.5, 2.0, and 3.0 m. In addition to application of Eqs. (4) to (7), in the case of snow-covered ice we calculated the conductive heat flux using a piece-wise linear approximation (Makshtas, 1991):

$$\mathrm{C} = -\mathrm{k_i}\ (\mathrm{T_s} - \mathrm{T_b}) / \left[\mathrm{h_i} + (\mathrm{k_i} - \mathrm{k_s}) / \mathrm{h_s}\right] \tag{8}$$

where k_s stands for heat conductivity of snow and h_s for snow thickness. The results suggest that for ice thicknesses less than 2 m, the existence of the snowpack controls the direction of SHF: for 1 m sea ice, SHF is -13 W m^{-2} (upwards) without snowpack but 5 W m^{-2} (downwards) with snow pack (Figure 9 b). For larger ice thicknesses, the impact of the snowpack decreases, as the insulating effect of the ice increases. In February conditions in the Central Arctic, the air specific humidity and saturation specific humidity over thick ice/snow are so small, that LHF ranged between -1 and 1 W m^{-2} (not shown).

4 Discussion

4.1 Differences between reanalyses, their importance, and consequences

In most Arctic basins, we found the highest SIC in NCEP/CFSR and JRA-55 data, whereas the values in ERA5 and MERRA-2 were lower and close to each other. The magnitude of the differences was up to 0.15, but typically around 0.05 (Figure 2), similar to the average differences between reanalyses in the Arctic Ocean shown in Collow et al. (2020). Differences in SIC of the order of 0.05 to 0.15 may generate large differences in turbulent surface fluxes, and the magnitude of these differences depends on the sensitivity of the fluxes to SIC. Our results indicated the highest sensitivity in November–April (Figures 4, 6, S4, and S7): approximately 400 W m^{-2} in LHF and over 800 W m^{-2} SHF per unit of SIC (change of SIC from 0 to 1). These values varied between the reanalyses – e.g. for LHF in November–December–January, in ERA5, JRA-55, and MERRA-2, they were approximately 200–300 W m^{-2} per unit of SIC, whereas they were as large as up to 600 W m^{-2} LHF per unit of SIC in NCEP/CFSR data. In warmer seasons, the sensitivity of turbulent surface fluxes to SIC was generally lower.

The differences in LHF and SHF, generated by differences in SIC and flux parameterisations, have strong impacts on the atmosphere, above all in cold-season conditions (November–April) when the SIC is close to one. According to modelling experiments by Lüpkes et al. (2008), in winter under clear skies, a SIC decrease of 1 % caused a T_{10m} increase of 3.5 K when the air mass flew long enough (48 h) over the zone of a high SIC. During cold-air outbreaks from the Antarctic sea ice zone, modelled T_{2m} may vary by more than 10 K depending on the SIC algorithm applied as seen in Figure 7 in Valkonen et al. (2008). Warming of the near-surface temperature caused by low sea-ice concentration then reduces the stratification in the Arctic ABL and makes the atmosphere more prone to cyclogenesis (Jaiser et al., 2012). Such local and regional impacts in the sea ice zone may have far-reaching effects beyond the polar regions. Sea-ice decline in the Arctic contributes to the Arctic amplification of climate warming, reducing the meridional temperature gradient between the Arctic and mid-latitudes. This impacts mid-latitude weather and climate, although the magnitude of the impacts and their distinction from natural variability is still under debate (Cohen et al., 2020).

4.2 Simplification of the sea ice in reanalyses and its impact on surface turbulent fluxes

The SIC in reanalyses does not include information on the spatial distribution of sea ice and open water within a grid cell. For example, if SIC is 0.5 we do not know whether there is a distinct ice margin dividing the grid cell in equal portions of sea ice and open water or if there are numerous small leads whose total area sums up to half of the grid cell. The impacts of the ice-water

distribution on turbulent surface fluxes may depend on the season, region, and weather conditions via complex interaction of processes. In the case of cold-air outbreaks in cold seasons, when the sensitivity of SHF and LHF to SIC is largest, a distinct ice margin (with only sea ice on one side and only open water on the other side) typically results in a situation when SHF and LHF are largest right downwind of the ice margin, and then decrease with fetch over the open ocean, as the near-surface air becomes warmer and more humid (e.g. Lüpkes and Schlünzen (1996)). In a similar weather situation but with the SIC associated with a series of narrow leads, the near-surface air is not expected to get as warm and moist, because part of the heat and moisture is returned to ice via downward turbulent fluxes over the patches of ice in between the leads, which allows larger SHF and LHF over the leads. However, comparing the turbulent surface fluxes averaged over the grid cell between these two exemplary cases would require sophisticated large-eddy simulation experiments. A theoretical argument favouring larger grid-averaged fluxes in the latter case is that the alternations between the leads and sea ice increase the surface roughness due to the form drag generated by floe edges (Lüpkes and Gryanik, 2015). This enhances the turbulent transfer not only for momentum but also for sensible and latent heat (Elvidge et al., 2023). In any case, even if the reanalysis products would include information on the spatial distributions of sea ice and open water within a grid cell, the SIC itself is an a oversimplification of the true situation, where the sea ice in a grid cell typically has a range of thicknesses, each with different surface temperature and, hence, SHF and LHF.

SIC in reanalyses is mostly based on satellite passive microwave data (Table 2). These data have typical spatial resolution of the order of 10 to 30 km, depending on the wavelength band. Hence, the observations do not detect narrow leads. Further, the SIC based on satellite data is sensitive to the processing algorithm applied (Spreen et al., 2008), and includes errors, e.g. due to atmospheric disturbances (Svendsen et al., 1987). Other satellite-based SIC products, such as thermal infrared data (Qiu et al., 2023) and data from Synthetic Aperture Radar (Park et al., 2020), are available at much higher spatial resolutions, with a pixel size of the order of tens of metres. However, the temporal and spatial coverage of these data sets are limited compared to the multi-decadal and global scales required for atmospheric reanalyses.

In addition to the uncertainty in SIC, there are also factors generating errors in the turbulent fluxes over leads. A source of biases in SHF and LHF is the thin ice cover, which is typical on winter leads but ignored in reanalyses. According to our calculations, ignoring the thin ice may cause an overestimation of the heat loss from the lead by several tens of W m^{-2} in February conditions in the Central Arctic. In warmer seasons, the effect is naturally smaller, and disappears in the peak of summer. Another source of biases in ERA5 and JRA-55 is the lack of snow on top of thick sea ice. Our calculations suggest that the local effect is smaller than that of the lack of thin ice on leads. However, as the lead fraction in the Central Arctic is small, we suppose that the regional effect of the lack of snow on thick sea ice is larger.

4.3 Other uncertainties in parameterization of surface turbulent fluxes

Even with perfect information on SIC, thin ice on leads, and the snow on top of ice, uncertainties are generated via application of Eqs. (1) and (2). The Numerical Weather Prediction (NWP) models used in the production of reanalyses have mutual differences in the height of their lowest atmospheric level. This height affects the differences between the atmospheric and surface values and the lowest level should be located within a layer where the turbulent fluxes can be assumed constant in

height. However, in stably stratified conditions, this layer is very shallow, and often does not reach the lowest model level. In such cases, the Monin-Obukhov similarity theory (the basis for Eqs. (1) and (2)) is not valid. Further, the vertical distribution of heat and moisture originating from leads (Lüpkes et al., 2012) cannot be correctly simulated if the model vertical resolution is coarse. Stable stratification also generates a lot of uncertainty in the turbulent exchange coefficient for heat and moisture (Andreas et al. (2010); Grachev et al. (2012)). In particular, the transition from weakly stable to very stable stratification results in a decrease in the magnitude of SHF even if the temperature difference between the air and the surface increases (Malhi, 1995), which may result in uncertainties up to 10–20 K in T_{2m} (Uppala et al., 2005). Another uncertainties arise from the effect of form drag, generated by flow edges, ridges, and sastrugi on the turbulent exchange coefficients (Andreas (1995); Lüpkes and Gryanik (2015); Elvidge et al. (2023)). Finally, the flux parameterisation includes an error source related to the limited representativeness of the grid-averaged values of air potential temperature, specific humidity and wind speed for the local conditions over the ice-covered and open-water parts of the grid cell (Vihma et al., 1998).

Another issue in reanalyses is the very common warm bias in both T_s (Herrmannsdörfer et al., 2023) and T_{2m} (Graham et al., 2019), especially during clear-sky events in cold season in the Arctic. If the biases in T_s and T_{2m} are approximately equal, the SHF over sea ice is not much affected. However, a positive T_{2m} bias reduces the temperature difference between the open water and the air above, resulting in underestimation of upward turbulent fluxes over leads. In summer, T_s over leads may be lower than T_{2m}, causing locally stable stratification, however, the summertime thermal differences between the atmosphere, sea ice, and leads are typically so small that the flux magnitudes and, hence, their absolute errors remain small. There is potential to reduce the biases in T_s, T_{2m} ,SHF, and LHF by corrections via machine-learning algorithms – trained by, e.g., satellite observations of the ice surface temperatures as shown in Zampieri et al. (2023).

4.4 Role of sea-ice concentration and meteorological variables on surface turbulent fluxes

Comparing the effects of SIC and other factors on LHF and SHF (Figures 8, S10-S24), it is evident that air-surface differences in temperature and specific humidity explain the flux variations better than SIC does. This is natural, as the air-surface differences are the basis for flux parameterisations in models. However, SIC plays a key role in controlling the surface temperature and the surface (saturation) specific humidity, which have constant (freezing-point related) values over areas of open water in the sea-ice zone (farther south, the sea surface temperature may strongly exceed the freezing point). Accordingly, the air-surface differences in temperature and specific humidity are strongly affected by SIC. Wind speed explained only 10 to 20 % of the turbulent surface fluxes variances, which we interpret as follows. Under constant air-surface differences in temperature and specific humidity, the magnitude of turbulent fluxes increases with increasing wind speed, as seen from Eqs. (1) and (2). However, in events of upward fluxes, the wind effect results in decrease of the fluxes, whereas in events of downward fluxes, the fluxes increase. The cancelling effects keep the degree of explanation small. It does not vanish because events with a high air temperature and specific humidity over the Arctic Ocean typically occur under strong winds (Walsh and Chapman (1998); Vihma and Pirazzini (2005)), favouring increase of the downward turbulent fluxes.

4.5 Decadal changes

As expected, all four reanalyses agreed on the general decrease of SIC over the 42-year study period. However, anomalies occurred in the Central Arctic and some of the adjacent seas in the cold season (November–April), where SIC remained the same or became higher in the second study period, by up to 2 % of the value in 1980–2000. These results are likely connected to the thinning of the Arctic sea ice in recent decades, which makes it more prone to ridging, rafting, and fast drift (Rampal et al., 2009). The exact mechanisms for the SIC increase remain unclear, but possibilities include regionally increased convergence of ice drift, associated with the closing of leads. Although in August–September–October in the Barents and Kara Seas the sea-ice decline has been very large (Table 3), we did not detect the same or just a very minor signal in the decadal increase of negative LHF and SHF (Tables 4 and S1). We interpret this as a consequence of increased transport of moist, warm air masses to the Arctic (Woods and Caballero, 2016) also associated with increasingly meridional cyclone tracks (Wickström et al., 2020). We found that the effect of SIC on both LHF and SHF weakened between the study periods in most areas of the Arctic, mostly in the Central Arctic, however, we found areas of increased effect of SIC on LHF and SHF between 1980–2000 and 2001–2021. The mechanisms of these changes in effects of SIC on turbulent surface fluxes are described more in detail in subsection 3.2.

The results generally indicated signs of decadal-scale improvement in the mutual agreement between reanalyses. The magnitudes of the Mean Biases in LHF and SHF between NCEP/CFSR and other reanalyses have decreased in nearly all basins and seasons. As the model and data assimilation system is the same over the entire reanalysis period, the better agreement may result from more data available for assimilation. This must be mostly due to more available satellite data, as increases in the amount of in-situ observations from the Arctic have been restricted to short periods, such as The Year of Polar Prediction (YOPP) Special Observation Periods in February–March and July–September in 2018 and The Multidisciplinary drifting Observatory for the Study of Arctic Climate (MOSAiC) field campaign in 2019–2020.

5 Conclusion

Our study expanded the knowledge on the effects of Arctic sea-ice concentration on the turbulent surface fluxes of sensible and latent heat, as represented in four global atmospheric reanalyses. We quantified the uncertainties in these effects arising from differences in SIC and in the sensitivity of the turbulent surface fluxes to SIC – analyses that have not been performed before. Because atmospheric reanalyses provide the best available information in data-sparse regions such as the Arctic and because the Arctic amplification of climate warming is thought to be primarily surface-based, it is important to quantify the differences in the representation of the Arctic surface energy budget and its sensitivity to SIC in these data sets. In the present study, we showed that the largest differences in effects of SIC on LHF and SHF in reanalyses come from the representation of the sea ice, which is modelled in NCEP/CFSR and oversimplified in ERA5, JRA-55, and MERRA-2. This difference in representation of the sea ice resulted generally in much higher sensitivity of turbulent surface fluxes to SIC in NCEP/CFSR (which assimilates both modelled sea-ice thickness and snow depth on the sea ice and accounts for their insulating effects) compared to other reanalyses with constant sea-ice thickness and no account for the snow on sea ice. A logical next step in our work is to study

the relationships of Arctic SIC and radiative surface fluxes and clouds in atmospheric reanalyses ERA5, JRA-55, MERRA-2, and NCEP/CFSR.

Code and data availability. https://doi.org/10.5281/zenodo.7978071, https://doi.org/10.5281/zenodo.7965919, https://a3s.fi/uhlitere-2000789-pub/* (To download a desired file, the name of it must be entered after the last forward slash, instead of *. Names of files can be found in codes or in the list of files at https://a3s.fi/swift/v1/AUTH_ea49151ae29449449d8e7cde1367e03a/uhlitere-2000789-pub/. Data description can be found at https://a3s.fi/uhlitere-2000789-pub/README_data.odt)

Author contributions. TU prepared the manuscript with contributions of TV, PU, and AK. TV designed the concept of the study with contributions of PU, AK, and TU. PU developed the code with the contribution of TU. TU collected and processed data and performed analyses.

Competing interests. The authors declare that they have no conflict of interest.

Acknowledgements. TU is a University-funded Doctoral Researcher at the University of Helsinki. The work of AK, PU, and TV was supported by the European Commission, Horizon 2020 Framework Programme (PolarRES; grant no. 101003590).

Hersbach et al. (2023) was downloaded from the Copernicus Climate Change Service (C3S) Climate Data Store (2023). The results contain modified Copernicus Climate Change Service information 2022. Neither the European Commission nor ECMWF is responsible for any use that may be made of the Copernicus information or data it contains. Furthermore, we acknowledge the providers of the data of the other three reanalyses used in our study: Japan Meteorological Agency, the National Center for Atmospheric Research (JRA-55, NCEP/CFSR, CFSv2), and the Global Modeling and Assimilation Office (MERRA-2).

References

References

Alam, A. and Curry, J.: Determination of surface turbulent fluxes over leads in Arctic sea ice, J. Geophys. Res., 102, 3331–3343, https://doi.org/10.1029/96JC03606, 1997.

Andreas, E. L.: Air-ice drag coefficients in the western Weddell Sea: 2. A model based on form drag and drifting snow., Journal of Geophysical Research, 100, https://doi.org/10.1029/94JC02016, 1995.

Andreas, E. L., Paulson, C. A., William, R. M., Lindsay, R. W., and Businger, J. A.: The turbulent heat flux from arctic leads, Boundary-Layer Meteorology, 17, 57–91, https://doi.org/10.1007/BF00121937, 1979.

Andreas, E. L., Persson, P. O. G., Grachev, A. A., Jordan, R. E., Horst, T., Guest, P. S., and Fairall, C.: Parameterizing Turbulent Exchange over Sea Ice in Winter, J. Hydrometeorol, 11, 87–104, https://doi.org/10.1175/2009JHM1102.1, 2010.

Aue, L., Vihma, T., Uotila, P., and Rinke, A.: On the warm bias in atmospheric reanalyses induced by the missing snow over Arctic sea-ice, Geophysical Research Letters, 49, https://doi.org/10.1029/2022GL100051, 2022.

Boggs, P. T., Donaldson, J. T., Schnabel, R. B., and Spiegelman, C. H.: A Computational Examination of Orthogonal Distance Regression, Journal of Econometrics, 38, 169–201, https://www.sciencedirect.com/science/article/pii/0304407688900322, 1988.

Bosilovich, M. G., Akella, S., and Coy, L. e. a.: MERRA-2: Initial evaluation of the climate, https://gmao.gsfc.nasa.gov/pubs/docs/Bosilovich803.pdf, 2015.

Bretherton, C. S., Widmann, M., Dymnikov, V. P., Wallace, J. M., and Bladé, I.: The Effective Number of Spatial Degrees of Freedom of a Time-Varying Field, Journal of Climate, 12, 1990–2009, https://journals.ametsoc.org/view/journals/clim/12/7/1520-0442_1999_012_1990_tenosd_2.0.co_2.xml, 1999.

Claussen, M.: Local advection processes in the surface layer of the marginal ice zone, Boundary-Layer Meteorol, 54, 1–27, https://doi.org/10.1007/BF00119409, 1991.

Cohen, J., Zhang, X., Francis, J., Jung, T., Kwok, R., Overland, J., Ballinger, T. J., Bhatt, U. S., Chen, H. W., Coumou, D., Feldstein, S., Gu, H., Handorf, D., Henderson, G., Ionita, M., Kretschmer, M., Laliberte, F., Lee, S., Linderholm, H. W., Maslowski, W., Peings, Y., Pfeiffer, K., Rigor, I., Semmler, T., Stroeve, J., Taylor, P. C., Vavrus, S., Vihma, T., Wang, S., Wendisch, M., Wu, Y., and Yoon, J.: Divergent consensuses on Arctic amplification influence on midlatitude severe winter weather., Nature climate change, pp. 20–29, https://doi.org/10.1038/s41558-019-0662-y, 2020.

Collow, A. B. M., Cullather, R. I., and Bosilovich, M. G.: Recent Arctic Ocean Surface Air Temperatures in Atmospheric Reanalyses and Numerical Simulations, Journal of Climate, 33, 4347–4367, https://journals.ametsoc.org/view/journals/clim/33/10/jcli-d-19-0703.1.xml, 2020.

Dai, A., Luo, D., Song, M., and Liu, J.: Arctic amplification caused by sea-ice loss under increasing CO2., Nature communications, 10, https://doi.org/10.1038/s41467-018-07954-9, 2002.

ECMWF: IFS Documentation CY41R2 - Part IV: Physical Processes, 4, ECMWF, https://doi.org/10.21957/tr5rv27xu, 2016.

Elvidge, A. D., Renfrew, I. A., Edwards, J. M., Brooks, I. M., Srivastava, P., and Weiss, A. I.: Improved simulation of the polar atmospheric boundary layer by accounting for aerodynamic roughness in the parameterization of surface scalar exchange over sea ice., Journal of Advances in Modeling Earth Systems, 15, https://doi.org/10.1029/2022MS003305, 2023.

Gelaro, R., McCarthy, W., and Suárez, M. J. e. a.: The Modern-Era Retrospective Analysis for Research and Applications, Version 2 (MERRA-2), Journal of Climate, 30, 5419–5454, 2017.

GMAO, Global Modeling, A. O.: Tavg1_2d_flx_Nx: MERRA-2 2D, 1-Hourly, Time-Averaged, Single-Level Assimilation, Single-Level Diagnostics., https://doi.org/10.5067/7MCPBJ41Y0K6, 2015a.

GMAO, Global Modeling, A. O.: Tavg1_2d_slv_Nx: MERRA-2 2D, 1-hourly, Time-Averaged, Single-Level Assimilation,Surface Flux Diagnostics V5.12.4, https://doi.org/10.5067/VJAFPLI1CSIV, 2015b.

Good, S., Fiedler, E., Mao, C., Martin, M. J., Maycock, A., Reid, R., Roberts-Jones, J., Searle, T., Waters, J., While, J., and Worsfold, M.: The Current Configuration of the OSTIA System for Operational Production of Foundation Sea Surface Temperature and Ice Concentration Analyses, Remote Sensing, 12, https://www.mdpi.com/2072-4292/12/4/720, 2020.

Grachev, A. A., Andreas, E. L., Fairall, C., Guest, P. S., and Persson, P. O. G.: Outlier problem in evaluating similarity functions in the stable atmospheric boundary layer, Bound.-Layer Meteorol., 144, 137–155, 2012.

Graham, R. M., Cohen, L., Ritzhaupt, N., Segger, B., Graversen, R. G., Rinke, A., Walden, V. P., Granskog, M. A., and Hudson, S. R.: Evaluation of Six Atmospheric Reanalyses over Arctic Sea Ice from Winter to Early Summer., Journal of Climate, 32, 4121–4143, https://doi.org/10.1175/JCLI-D-18-0643.1, 2019.

Gultepe, I., Isaac, G. A., Williams, A., Marcotte, D., and Strawbridge, K. B.: Turbulent heat fluxes over leads and polynyas, and their effects on arctic clouds during FIRE.ACE: Aircraft observations for April 1998, Atmosphere-Ocean, https://doi.org/10.3137/ao.410102, 2003.

Herrmannsdörfer, L., Müller, M., Shupe, M. D., and Rostosky, P.: Surface temperature comparison of the Arctic winter MOSAiC observations, ERA5 reanalysis, and MODIS satellite retrieval., Elementa: Science of the Anthropocene, 11, https://doi.org/10.1525/elementa.2022.00085, 2023.

Hersbach, H., Bell, B., Berrisford, P., Hirahara, S., Horányi, A., Muñoz Sabater, J., Nicolas, J., Peubey, C., Radu, R., Schepers, D., Simmons, A., Soci, C., Abdalla, S., Abellan, X., Balsamo, G., Bechtold, P., Biavati, G., Bidlot, J., Bonavita, M., and Thépaut, J.-N.: The ERA5 global reanalysis, Quarterly Journal of the Royal Meteorological Society, https://doi.org/10.1002/qj.3803, 2020.

Hersbach, H., Bell, B., Berrisford, P., Biavati, G., Horányi, A., J., M. S., Nicolas, J., Peubey, C., Radu, R., Rozum, I., Schepers, D., Simmons, A., Soci, C., Dee, D., and Thépaut, J.-N.: ERA5 hourly data on single levels from 1940 to present., https://doi.org/10.24381/cds.adbb2d47, 2023.

Iribarne, J. and Godson, W.: Atmospheric Thermodynamics, D. Reidel Publishing Company, 1973.

Ishii, M., Shouji, A., Sugimoto, S., and Matsumoto, T.: OBJECTIVE ANALYSES OF SEA-SURFACE TEMPERATURE AND MARINE METEOROLOGICAL VARIABLES FOR THE 20TH CENTURY USING ICOADS AND THE KOBE COLLECTION., International Journal of Climatology, 25, 865–879, https://rmets.onlinelibrary.wiley.com/doi/10.1002/joc.1169, 2005.

Jaiser, R., Dethloff, K., Handorf, D., and Cohen, J.: Impact of sea ice cover changes on the Northern Hemisphere atmospheric winter circulation, Tellus A: Dynamic Meteorology and Oceanography, 64, https://doi.org/10.3402/tellusa.v64i0.11595, 2012.

JMA, J. M. A.: JRA-55: Japanese 55-year Reanalysis, Daily 3-Hourly and 6-Hourly Data., https://doi.org/10.5065/D6HH6H41, 2013.

Kobayashi, S., Ota, Y., and Harada, Y. e. a.: The JRA-55 Reanalysis: General Specifications and Basic Characteristics, Journal of the Meteorological Society of Japan, 93, 5–48, https://doi.org/10.2151/JMSJ.2015-001, 2015.

Koster, R. D. and Suarez, M. J.: Modeling the land surface boundary in climate models as a composite of independent vegetation stands, J. Geophys. Res., 97, 2697—-2715, 1992.

Lim, W.-I., Park, H.-S., Stewart, A. L., and Seo, K.-H.: Suppression of Arctic sea ice growth in the Eurasian–Pacific seas by winter clouds and snowfall, Journal of Climate, 35, 669–686, https://doi.org/10.1175/JCLI-D-21-0282.1, 2022.

Lindsay, R., Wensnahan, M., Schweiger, A., and Zhang, J.: Evaluation of Seven Different Atmospheric Reanalysis Products in the Arctic., Journal of Climate, 27, 2588–2606, https://doi.org/10.1175/JCLI-D-13-00014.1, 2014.

Lüpkes, C. and Gryanik, V.: A stability-dependent parametrization of transfer coefficients for momentum and heat over polar sea ice to be used in climate models., Journal of Geophysical Research, 120, https://doi.org/10.1002/2014JD022418, 2015.

Lüpkes, C. and Schlünzen, K. H.: Modelling the Arctic Convective Boundary-Layer with Different Turbulence Parameterizations., Boundary-Layer Meteorol., 79, 1996.

Lüpkes, C., Vihma, T., Birnbaum, G., and Wacker, U.: Influence of leads in sea ice on the temperature of the atmospheric boundary layer during polar night., Geophys. Res. Lett., 35, https://doi.org/10.1029/2007GL032461, 2008.

Lüpkes, C., Vihma, T., Birnbaum, G., Dierer, S., Garbrecht, T., Gryanik, V., Gryschka, M., Hartmann, J., Heinemann, G., Kaleschke, L., Raasch, S., Savijärvi, H., Schlünzen, K., and Wacker, U.: Mesoscale modelling of the Arctic atmospheric boundary layer and its interaction with sea ice, in: Arctic Climate Change - The ACSYS Decade and Beyond, edited by Lemke, P. and Jacobi, H.-W., vol. 43, Atmospheric and Oceanographic Sciences Library, 2012.

Makshtas, A. P.: The heat budget of the Arctic ice in the winter., Cambridge, International Glaciological Society, 1991.

Maksimovich, E. and Vihma, T.: The effect of surface heat fluxes on interannual variability in the spring onset of snow melt in the central Arctic Ocean, Journal of Geophysical Research: Oceans, 117, https://doi.org/10.1029/2011JC007220, 2012.

Malhi, Y. S.: The significance of the dual solutions for heat fluxes measured by the temperature fluctuation method in stable conditions, Boundary-Layer Meteorol., 74, 389–396, 1995.

Matsumoto, T., Ishii, M., Fukuda, Y., and Hirahara, S.: Sea ice data derived from microwave radiometer for climate monitoring. Proceedings of the 14th Conference on Satellite Meteorology and Oceanography, Atlanta, USA., in: Presented at the 14th Conference on Satellite Meteorology and Oceanography, https://ams.confex.com/ams/Annual2006/techprogram/paper_101105.htm, 2006.

Michaelis, J., Lüpkes, C., Schmitt, A., and Hartmann, J.: Modelling and parametrization of the convective flow over leads in sea ice and comparison with airborne observations, Quarterly Journal of the Royal Meteorological Society, 147, https://doi.org/10.1002/qj.3953, 2021.

Morice, C. P., Kennedy, J. J., Rayner, N. A., W., P., J., Hogan, E., and Killick, R. E., e. a.: An updated assessment of near-surface temperature change from 1850: the HadCRUT5 data set., Journal of Geophysical Research: Atmospheres, 126, https://doi.org/10.1029/2019JD032361, 2021.

Overland, J. E., McNutt, S. L., Groves, J., Salo, S., Andreas, E. L., and Persson, P. O. G.: Regional sensible and radiative heat flux estimates for the winter arctic during the Surface Heat Budget of the Arctic Ocean (SHEBA) experiment, J. Geophys. Res., 105, 14 093—14 102, 2000.

Park, J.-W., Korosov, A. A., Babiker, M., Won, J.-S., Hansen, M. W., and Kim, H.-C.: Classification of sea ice types in Sentinel-1 synthetic aperture radar images, The Cryosphere, 14, https://doi.org/10.5194/tc-14-2629-2020, 2020.

Perovich, D. K., Light, B., Eicken, H., Jones, K. F., Runciman, K., and Nghiem, S. V.: Increasing solar heating of the Arctic Ocean and adjacent seas, 1979–2005: Attribution and role in the ice-albedo feedback, The Cryosphere, 34, https://doi.org/10.1029/2007GL031480, 2007.

Persson, P. O. G., W., F. C., L., A. E., Guest, P. G., and Perovich, D. K.: Measurements near the Atmospheric Surface Flux Group tower at SHEBA: Near-surface conditions and surface energy budget, J. Geophys. Res., 107, https://agupubs.onlinelibrary.wiley.com/doi/pdf/10.1029/2000JC000705, 2002.

Petrich, C., Langhorne, P. J., and Haskell, T. G.: Formation and structure of refrozen cracks in land-fast first-year sea ice, J. Geophys. Res., 112, https://doi.org/10.1029/2006JC003466, 2007.

Qiu, Y., Li, X.-M., and Guo, H.: Spaceborne thermal infrared observations of Arctic sea ice leads at 30 m resolution, The Cryosphere, 17, 2829–2849, https://doi.org/10.5194/tc-17-2829-2023, 2023.

Rampal, P., Weiss, J., and Marsan, D.: Positive trend in the mean speed and deformation rate of Arctic sea ice: 1979–2007, J. Geophys. Res., 114, 2009.

Saha, S., Moorthi, S., Pan, H.-L., Wu, X., Wang, J., Nadiga, S., Tripp, P., Kistler, R., Woollen, J., Behringer, D., Liu, H., Stokes, D., Grumbine, R., Gayno, G., Wang, J., Hou, Y.-T., Chuang, H.-Y., Juang, H.-M., Sela, J., and Goldberg, M.: The NCEP climate forecast system reanalysis, Bulletin of The American Meteorological Society, 91, https://doi.org/10.1175/2010BAMS3001.1, 2010.

Saha, S., Moorthi, S., Pan, H.-L., Wu, X., Wang, J., Nadiga, S., Tripp, P., Kistler, R., Woollen, J., Behringer, D., Liu, H., Stokes, D., Grumbine, R., Gayno, G., Wang, J., Hou, Y.-T., Chuang, H.-Y., Juang, H.-M. H., Sela, J., Iredell, M., Treadon, R., Kleist, D., Van Delst, P., Keyser, D., Derber, J., Ek, M., Meng, J., Wei, H., Yang, R., Lord, S., van den Dool, H., Kumar, A., Wang, W., Long, C., Chelliah, M., Xue, Y., Huang, B., Schemm, J.-K., Ebisuzaki, W., Lin, R., Xie, P., Chen, M., Zhou, S., Higgins, W., Zou, C.-Z., Liu, Q., Chen, Y., Han, Y., Cucurull, L., Reynolds, R. W., Rutledge, G., and Goldberg, M.: NCEP Climate Forecast System Reanalysis (CFSR) 6-hourly Products, January 1979 to December 2010., https://doi.org/10.5065/D69K487J, 2010.

Saha, S., Moorthi, S., Pan, H.-L., Wu, X., Wang, J., Nadiga, S., Tripp, P., Kistler, R., Woollen, J., Behringer, D., Liu, H., Stokes, D., Grumbine, R., Gayno, G., Wang, J., Hou, Y.-T., Chuang, H.-Y., Juang, H.-M. H., Sela, J., Iredell, M., Treadon, R., Kleist, D., Van Delst, P., Keyser, D., Derber, J., Ek, M., Meng, J., Wei, H., Yang, R., Lord, S., van den Dool, H., Kumar, A., Wang, W., Long, C., Chelliah, M., Xue, Y., Huang, B., Schemm, J.-K., Ebisuzaki, W., Lin, R., Xie, P., Chen, M., Zhou, S., Higgins, W., Zou, C.-Z., Liu, Q., Chen, Y., Han, Y., Cucurull, L., Reynolds, R. W., Rutledge, G., and Goldberg, M.: NCEP Climate Forecast System Version 2 (CFSv2) 6-hourly Products., https://doi.org/10.5065/D61C1TXF, 2011.

Saha, S., Moorthi, S., Wu, X., Wang, J., Nadiga, S., Tripp, P., Behringer, D., Hou, Y.-T., ya Chuang, H., Iredell, M., Ek, M., Meng, J., Yang, R., Mendez, M. P., van den Dool, H., Zhang, Q., Wang, W., Chen, M., and Becker, E.: The NCEP Climate Forecast System Version 2, Journal of Climate, 27, 2185 – 2208, https://journals.ametsoc.org/view/journals/clim/27/6/jcli-d-12-00823.1.xml, 2014.

Screen, J. A. and Simmonds, I.: The central role of diminishing sea ice in recent Arctic temperature amplification, Nature, 646, 1334–1337, https://doi.org/10.1038/nature09051, 2010.

Serreze, M. C., Barrett, A. P., Stroeve, J. C., Kindig, D. N., and Holland, M. M.: The emergence of surface-based Arctic amplification, The Cryosphere, 3, 11–19, https://tc.copernicus.org/articles/3/11/2009/tc-3-11-2009.pdf, 2009.

Spreen, G., Kaleschke, L., and Heygster, G.: Sea ice remote sensing using AMSR-E 89-GHz channels, Journal of Geophysical Research, 113, https://doi.org/10.1029/2005JC003384, 2008.

Svendsen, E., Matzler, C., and Grenfell, T. C.: A model for retrieving total sea ice concentration from a spaceborne dual-polarized passive microwave instrument operating near 90 GHz, Int J. Remote Sensing, 8, https://doi.org/10.1080/01431168708954790, 1987.

Taylor, K. E., Williamson, D., and Zwiers, F.: The sea surface temperature and sea-ice concentration boundary conditions for AMIP II simulations, in: PCMDI Report No. 60, https://pcmdi.llnl.gov/report/ab60.html, 2000.

Tsamados, M., Feltham, D., Petty, A., Schroeder, D., and Flocco, D.: Processes controlling surface, bottom and lateral melt of Arctic sea ice in a state of the art sea ice model, Phil. Trans. R. Soc. A, http://doi.org/10.1098/rsta.2014.0167, 2015.

Uppala, S. M., KÅllberg, P. W., Simmons, A. J., Andrae, U., Bechtold, V. D. C., Fiorino, M., Gibson, J. K., Haseler, J., Hernandez, A., Kelly, G. A., Li, X., Onogi, K., Saarinen, S., Sokka, N., Allan, R. P., Andersson, E., Arpe, K., Balmaseda, M. A., Beljaars, A. C. M., Berg, L. V. D., Bidlot, J., Bormann, N., Caires, S., Chevallier, F., Dethof, A., Dragosavac, M., Fisher, M., Fuentes, M., Hagemann, S., Hólm, E., Hoskins, B. J., Isaksen, L., Janssen, P. A. E. M., Jenne, R., Mcnally, A. P., Mahfouf, J.-F., Morcrette, J.-J., Rayner, N. A.,

Saunders, R. W., Simon, P., Sterl, A., Trenberth, K. E., Untch, A., Vasiljevic, D., Viterbo, P., and Woollen, J.: The ERA-40 reanalysis, Quarterly Journal of the Royal Meteorological Society, 131, https://doi.org/10.1256/qj.04.176, 2005.

Valkonen, T., Vihma, T., and Doble, M.: Mesoscale modelling of the atmospheric boundary layer over the Antarctic sea ice: a late autumn case study, Mon. Wea. Rev., 136, 1457–1474, 2008.

Vihma, T.: Subgrid parameterization of surface heat and momentum fluxes over polar oceans, J. Geophys. Res., 100, 1995.

Vihma, T. and Pirazzini, R.: On the factors controlling the snow surface and 2-m air temperatures over the Arctic sea ice in winter, Bound.-Layer Meteorol., 117, 73–90, 2005.

Vihma, T., Uotila, J., and Launiainen, J.: Air-sea interaction over a thermal marine front in the Denmark Strait, J. Geophys. Res., 103, 1998.

Vihma, T., Jaagus, J., Jakobson, E., and Palo, T.: Meteorological conditions in the Arctic Ocean in spring and summer 2007 as recorded on the drifting ice station Tara, Geophys. Res. Lett., 35, https://doi.org/10.1029/2008GL034681, 2008.

Walden, V. P., Hudson, S. R., Cohen, L., Murph, S. Y., and Granskog, M. A.: Atmospheric components of the surface energy budget over young sea ice : Results from the N-ICE2015 campaign., J. Geophys. Res. Atmos., 122, 8427—-8446, https://doi.org/10.1002/2016JD026091, 2017.

Walsh, J. E. and Chapman, W. L.: Arctic Cloud–Radiation–Temperature Associations in Observational Data and Atmospheric Re-analyses, J. Climate, 11, 3030–3045, 1998.

Wei, Z., Zhang, Z., Vihma, T., Wang, X., and Chen, Y.: An overview of Antarctic polynyas: sea ice production, forcing mechanisms, temporal variability and water mass formation, Adv Polar Sci, 32, https://doi.org/10.13679/j.advps.2021.0026, 2021.

Wickström, S., Jonassen, M., Cassano, J. J., and Vihma, T.: Present temperature, precipitation and rain-on-snow climate in Svalbard, J. Geophys. Res. Atmospheres, 125, https://doi.org/10.1029/2019JD032155, 2020.

Woods, C. and Caballero, R.: The role of moist intrusions in winter Arctic warming and sea ice decline, J. Climate, 29, https://doi.org/10.1175/JCLI-D-15-0773.1, 2016.

Zampieri, L., Arduini, G., Holland, M., Keeley, S. P. E., Mogensen, K., Shupe, M. D., and Tietsche, S.: A Machine Learning Correction Model of the Winter Clear-Sky Temperature Bias over the Arctic Sea Ice in Atmospheric Reanalyses., Monthly Weather Review, 151, https://doi.org/10.1175/MWR-D-22-0130.1, 2023.